Coastal Engineering 58 (2011) 66–84

Contents lists available at ScienceDirect

Coastal Engineering

journal homepage: www.elsevier.com/locate/coastaleng

A Boussinesq-type wave driver for a morphodynamical model to predict short-term morphology

Ivo Wenneker [a,*], Ap van Dongeren [a], Jamie Lescinski [a], Dano Roelvink [a,b], Mart Borsboom [a]

[a] Deltares, P.O. Box 177, 2600 MH, Delft, The Netherlands
[b] UNESCO-IHE, P.O. Box 3015, 2601 DA, Delft, The Netherlands

ARTICLE INFO

Article history:
Received 16 March 2010
Received in revised form 2 July 2010
Accepted 17 August 2010

Keywords:
Bar morphology
Coastal processes
Boussinesq-type wave model
Delft3D
Low-frequency waves
Duck
Wave transformation
Undertow
Wave asymmetry
Velocity skewness
Nearshore circulation

ABSTRACT

The prediction of near-shore morphology on the time scale of a storm event and the length scale of a few surf zone widths is an active area of research. Intense wave breaking drives offshore-directed currents (undertow) carrying sediment seawards, resulting in offshore bar migration. In contrast, higher order nonlinear properties, such as wave asymmetry (velocity skewness) and velocity asymmetry, are drivers for shoreward transport. These wave processes are included in phase-resolving models such as Boussinesq-type wave models (e.g., TRITON). Short-wave averaging in the wave model yields wave-induced forces (e.g., radiation stress gradients) and a wave asymmetry term. The wave-induced forces are used in a hydrostatic model (e.g., Delft3D flow module) to drive the current and undertow, resulting in a 3D velocity profile. The wave model and hydrostatic model are coupled online with a morphodynamic model (e.g., Delft3D morphology module). The latter computes, based on the 3D flow profile and the wave asymmetry term, the sediment transport and performs the bathymetry updates. The updates are transferred directly back to the hydrodynamic models. The coupling of the wave model TRITON and the Delft3D modules is validated by comparing against extensive laboratory data sets (LIP and Boers) and a field case (Duck94), and show a good performance for the hydrodynamics and a reasonable/fair performance for the bar movements.

1. Introduction

The prediction of near-shore morphology on the time scale of a storm event and the length scale of a few surf zone widths is an active area of research and is of interest to shoreline management, for protection of the hinterland against flooding, recreational safety, and naval operations.

Within this time scale, rip channels can evolve and sand banks can migrate. These bathymetric changes are caused by waves and currents. In turn, waves and currents are affected by changes in the bathymetry. Hence, studying the beach profile evolution requires a coupling – preferably at a high rate of exchange of up-to-date data – between hydrodynamic models (waves and currents) and morphodynamic models (sediment transport and bathymetry updates).

As is well-known, intense wave breaking on sandbars drives offshore-directed currents (undertow). The latter carry sediment seawards, resulting in offshore bar migration. In contrast, higher order, nonlinear properties, such as wave asymmetry and skewness, are drivers for wave-averaged, shoreward transport (Hoefel and Elgar, 2003; Long et al., 2006; Hsu et al., 2006; Ruessink et al., 2007). Additional intra-wave properties, such as Stokes drift, boundary layer streaming, the generation of higher harmonics and bound long waves have also been found to have a strong impact on morphodynamic changes (Reniers et al. (2004a); Henderson et al., 2004; Trowbridge and Young, 1989).

These processes are included in phase-resolving wave models and need not be parameterized, as is required in phase-averaged wave models which would make such types of models suitable for application to this purpose. Furthermore, accurate modeling of wave dispersion and wave breaking is essential in the surf zone. A 2DH (2D in the horizontal) Boussinesq-type wave model such as TRITON (Borsboom et al. (2000, 2001a,b)); Groeneweg et al. (2002); Van Gent and Doorn (2001); Wenneker and Borsboom (2005)) can provide such an accurate modeling. However, morphodynamic computations over a longer time scale are computationally expensive with Boussinesq-type wave models, which is the reason why phase-averaged models have been commonly used for this purpose.

One such phase-averaged model is the flow module of the Delft3D model (Stelling, 1983; Lesser et al., 2004). It is based on the hydrostatic flow assumption and solves the short-wave averaged 3D shallow water equations. The model is capable of predicting infra-

* Corresponding author. Hydraulic Engineering, Deltares, P.O. Box 177, 2600 MH, Delft, The Netherlands. Tel.: +31 88 3358383; fax: +31 88 3358582.
E-mail addresses: ivo.wenneker@deltares.nl (I. Wenneker), ap.vandongeren@deltares.nl (A. van Dongeren), jamie.lescinki@deltares.nl (J. Lescinski), dano.roelvink@deltares.nl (D. Roelvink), mart.borsboom@deltares.nl (M. Borsboom).

0378-3839/$ – see front matter © 2010 Elsevier B.V. All rights reserved.
doi:10.1016/j.coastaleng.2010.08.007

wave effects (e.g. currents and long waves) directly, but not intra-wave aspects (e.g. short waves). This implies that wave properties on the intra-wave group scale need either be parameterized (e.g. the wave forcing through radiation stress gradients, which are a function of integral wave heights, and linear theory), or extracted from another source, the so-called “wave driver”. In this paper, we opt for the latter, and choose TRITON as the wave driver. This choice requires TRITON and the Delft3D model to run in parallel (simultaneously), exchanging information at given time instants.

There is a twofold motivation for coupling two existing hydrodynamic models – a 2DH wave model and a 3D flow model – instead of developing a 3D model for the computation of 3D intra-wave hydrodynamics. In the first place, coupling already existing and separately validated models is financially cheaper than developing a new model. In the second place, the CPU time of such a 3D model would be much larger than that of the coupled combination of the two models. This can be understood as follows: in the present field application, two distinct time and length scales can be identified, namely that of the individual wave and that of the wave group. CPU time is saved by computing the individual waves in a 2DH model instead of in a 3D model, only utilizing the 3D model to resolve the wave group scale.

Morphological computations not only require an accurate representation of the hydrodynamics – for which the coupling between TRITON and the Delft3D flow module is employed – but also of the sediment transport. The latter is computed using the Delft3D morphology module, with hydrodynamic input from TRITON and the Delft3D flow module. Hydrodynamic input is necessary, because suspended sediment transport is both wave- and current-driven. Evaluation of the current-driven suspended sediment transport requires the vertical distribution of the sediment concentration and the vertical velocity profile as input for the Delft3D morphology module (Lesser et al., 2004). The vertical velocity profile is computed in the Delft3D flow module, driven by the short-wave induced forces obtained in TRITON. The hydrodynamic component of the wave-driven suspended sediment transport (which includes the effects of wave asymmetry) is computed in TRITON as well. The bed-load transport can be computed in the Delft3D morphology module, employing parameterized intra-wave properties. However, we opted for direct computation of the bed-load transport in TRITON because it has the advantage of avoiding parameterization of the short waves. The bathymetry updates are done in the Delft3D morphology module, and transferred back to TRITON.

In the present paper, we describe the model set-up and results of model simulations of near-shore, short-term (on the time-scale of a storm) morphodynamics due to forcing by wind waves, by (locally generated) low-frequency waves and currents by combining the strengths of TRITON and the flow module and morphology module of Delft3D. In Van Dongeren et al. (2006), the first results of the proposed approach were given.

A similar approach to the one discussed in this paper is followed by Rakha et al. (1997). A major difference between our approach and that of Rakha et al. (1997), is that in our approach the vertical dimension is included in the model equations when required (e.g., in the flow and suspended sediment computation). In Hoefel and Elgar (2003), it is proposed to include fluid acceleration effects in waves to predict onshore sandbar migration and good results are obtained for the onshore bar migration event recorded at Duck, NC, USA. Lescinski and Özkan-Haller (2004) modeled the same Duck94 onshore bar migration events using a fully dispersive, nonlinear mild slope equation wave model in combination with an undertow and an energetics-type sediment transport models. They were also able to predict onshore-directed transport of the sandbar, and found that velocity asymmetry was a dominate process, but predicted a severe flattening of the bar. Additionally, they were also successful in predicting the offshore-directed bar migration observed during the same field experiment. In Hsu et al. (2006), several models were validated against the same bar migration event: the EEA (extended-energetics acceleration) model, based on Hoefel and Elgar (2003), the WRED (single-phase, wave-resolving eddy-diffusive) model, and the EEFF (extended energetics friction factor) model. It is concluded that these models predict the onshore bar migration with similar skill, so that it was inconclusive on which mechanisms between velocity asymmetry and velocity skewness actually dominate the sediment transport processes of cross-shore sand bar migration. Long et al. (2006) modified an existing Boussinesq-type wave model by incorporating the undertow contribution. Using laboratory data of the LIP11D experiments for validation, the model is used to drive a sediment transport model and to predict both an onshore bar migration event (LIP-1C), when non-linear wave processes dominate, and an offshore bar migration event (LIP-1B), when undertow dominates. The model again performed qualitatively well predicting the onshore bar migration, but lacked success when predicting the offshore migration.

The outline of this paper is as follows. In Section 2, the 2DH Boussinesq-type wave model TRITON is discussed. In Section 3, the hydrodynamic coupling between TRITON and the Delft3D flow module is introduced. The discussion focuses on aspects relevant for the present application: the derivation of expressions for the short-wave induced forces, and the distinction between organized and roller wave force. The Delft3D flow and morphology modules form the topic of Section 4. The coupling between TRITON and the Delft3D flow and morphology modules is discussed in Section 4 as well. In Section 5, several validation cases (LIP laboratory experiments, experiments as performed by Boers, and the Duck94 field experiment) are presented. Conclusions are gathered in Section 6.

2. Boussinesq-type wave model TRITON

2.1. Introduction

Boussinesq-type wave models are especially well suited for the simulation of wave propagation of short waves in relatively shallow regions, where nonlinear effects (e.g., wave breaking and generation of higher and lower harmonics), shoaling, diffraction, refraction and dispersion play an important role. In order to obtain an efficient formulation, Boussinesq-type wave models assume a vertical flow structure, i.e. the velocity profile across the depth is modeled analytically instead of calculated numerically. Hence, with a Boussinesq-type wave model the whole intra-wave and infra-wave range (waves and flow) can be computed.

The 2DH time-domain Boussinesq-type wave model TRITON is applied in the present paper as the wave driver, which ‘drives’ the currents and long waves, thereby ‘driving’ a large part of the sediment transport. More information on TRITON can be found in Borsboom et al. (2000, 2001a,b)), Groeneweg et al. (2002), Van Gent and Doorn (2001), Wenneker and Borsboom (2005), and Wenneker et al. (2006).

2.2. Model equations

The model formulation as discussed extensively in Borsboom et al. (2000) is summarized here. The depth-integrated continuity and momentum equations as employed in the 2DH time-accurate Boussinesq-type model TRITON are given by:

$$\frac{\partial H}{\partial t} + \nabla\cdot\mathbf{q} = 0, \tag{1}$$

$$\frac{\partial \mathbf{q}}{\partial t} + \nabla\cdot(\mathbf{uq}) + \nabla\left(\tfrac{1}{2}g\tilde{H}^2\right) - (gH + p_b)\nabla h + \nabla\cdot(H\boldsymbol{\tau}) = 0. \tag{2}$$

These equations are used in the given conservative form, implying that mass and momentum are conserved in the model simulations.

The meaning of the symbols is as follows: H the total water depth, t the time, $\nabla = (\partial/\partial x, \partial/\partial y)$ the horizontal gradient operator, $\mathbf{q}$ the depth-integrated velocity (flux), g the gravitational acceleration constant, and the water depth with respect to some arbitrary constant horizontal reference level. The notation of the convective term $\nabla\cdot(\mathbf{uq})$ may cause some trouble. The Cartesian tensor notation may relieve this. The time derivative term in expression (2) is, using this notation, written as $\partial q^{\alpha}/\partial t$, where superscript α denotes the considered horizontal coordinate (x or y). The convective term is written as $(u^{\beta}q^{\alpha})_{,\beta}$, where summation takes place over the horizontal coordinates β, and the subscript $(,\beta)$ implies a spatial derivative in β. The depth-averaged velocity is given by:

$$\mathbf{u} = \mathbf{q}/H. \tag{3}$$

The depth-averaged viscous stress tensor $\boldsymbol{\tau}$ is used to model wave breaking, further discussed in Section 2.3. The term gH represents the hydrostatic part of the pressure at the bottom (divided by the water density, which is assumed constant). The non-hydrostatic part of the pressure at the bottom (divided by the water density) is given by:

$$p_b = g\left(\frac{3}{2}\tilde{H} - \frac{3}{2}H + \frac{1}{4}H\nabla H\cdot\nabla\zeta\right), \tag{4}$$

where $\zeta = H - h$ denotes the water surface elevation with respect to the horizontal reference level. The variable $\tilde{H}$ represents the depth-averaged pressure (divided by the water density) and follows from:

$$\begin{aligned}\tilde{H} - \alpha H^2\nabla^2\tilde{H} - \beta H\nabla h\cdot\nabla\tilde{H} \\ = H - \left(\alpha - \frac{1}{3}\right)H^2\nabla^2 H - \left(\beta - \frac{1}{2}\right)H\nabla h\cdot\nabla H - \frac{1}{2}(\nabla h\cdot\nabla h)H - \frac{1}{3}\left(H\nabla^2 h\right)H.\end{aligned} \tag{5}$$

This expression consists of a hydrostatic and a non-hydrostatic component. This [2/2] Padé expression models dispersion and shoaling in a compact way, which reduces computing times and facilitates implementation. The values for α and β are 0.385 and 0.36, and are chosen such that they yield an optimal behaviour for linear dispersion and linear shoaling, see Borsboom et al. (2000). In case of long waves and currents (the long wave limit, $kh \to 0$), expression (5) reduces to the hydrostatic limit ($\tilde{H} \to H$). Note that, since only the gradients of ζ and h appear in the model equations, the formulation is independent of the reference level. This property, which facilitates the use of the model (e.g., inclusion of tides, which can be considered as a slow variation of the reference level), is often lost in other Boussinesq-type wave models due to the applied approximations, see Borsboom et al. (2000).

TRITON uses advanced techniques for the treatment of wave boundaries (enforcing the incoming wave signal, simultaneously preventing spurious reflection of outgoing waves) and landward boundaries (partial and full reflection). For more details on this subject, we refer to Borsboom et al. (2001a) and Wenneker and Borsboom (2005).

2.3. Wave breaking model

For reasons that will become clear in Section 3.3, we need to discuss the TRITON wave breaking model. The wave breaking model is a combination of the eddy viscosity concept and the roller concept. Conservation of momentum as in expression (2) ensures that the wave properties under breaking waves are modeled correctly and that the wave breaking model only dissipates wave energy. Here we restrict ourselves to discussing the 1D formulation of the wave breaking model, see also Borsboom et al. (2001b)).

Breaking of a wave which propagates into the positive x-direction is modeled by means of the following term in the momentum equation:

$$\frac{\partial}{\partial x}(H\tau_{xx}) = \frac{\partial}{\partial x}\left(2H\nu\frac{\partial u}{\partial x}\right), \tag{6}$$

with ν the turbulence eddy viscosity coefficient, and τ_{xx} is the component of the tensor $\boldsymbol{\tau}$ which is relevant for wave breaking of a wave propagating in the x-direction. For closure, the eddy viscosity coefficient needs to be specified. The surface roller model described by Schäffer et al. (1993) is employed for this. Wave breaking is assumed to initiate each time the slope angle of the local water surface in the direction of wave propagation exceeds a given value ϕ_{ini}. Once a wave starts breaking, a line is drawn at an angle ϕ that is tangent to the free surface at the toe of the roller, and that intersects the free surface at the back of the roller. The line is denoted by $\zeta_r = \zeta_r(x)$. After the moment t_{ini} of initiation of wave breaking, the slope angle φ is decreased gradually from its initial value ϕ_{ini} to its lower final value ϕ_{end} at a rate depending on time scale $t_{1/2}$:

$$\phi = \phi_{end} + (\phi_{ini} - \phi_{end})\exp\left[-\ln 2\frac{t - t_{ini}}{t_{1/2}}\right] \tag{7}$$

The vertical area in between the line and the free surface (see Fig. 1) is assumed to be proportional to the intensity of the surface roller. The eddy viscosity coefficient that is used in the present model is therefore scaled with the TRITON roller thickness $\delta^*(x) = \zeta(x) - \zeta_r(x)$ in this area:

$$\nu = f_p\delta^*(c_r - u), \tag{8}$$

where c_r is the wave celerity of the roller and f_p a dimensionless scaling parameter. Note that the δ^* used here should not be interpreted as the thickness of the turbulent wedge that occurs in physical reality; this issue is addressed in Section 3.3.

3. Coupling between the wave model and the flow model

3.1. Evaluation of short-wave induced forces

The Boussinesq-type wave model computes variables on the intra-wave time scale. These need to be short-wave averaged and compiled into wave forces which will be used to drive the long waves and currents in the Delft3D flow module. The following procedure is similar to the one given in Chapter 11 of Svendsen (2005). We introduce the separation of some TRITON variable φ into a slowly varying part $\overline{\varphi}$ (the component associated with long waves (including Stokes drift) and currents) and a fluctuating part φ' (the component associated with short waves):

$$\varphi = \overline{\varphi} + \varphi'. \tag{9}$$

By definition, the short-wave component satisfies:

$$\overline{\varphi'} = 0. \tag{10}$$

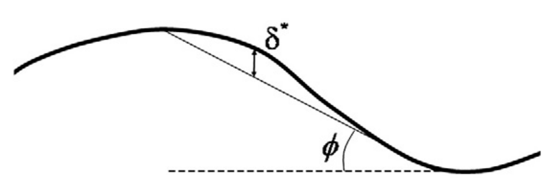

Fig. 1. Schematization of a roller.

Therefore, the following relation is automatically satisfied:

$$\overline{\overline{\varphi}} = \overline{\varphi}. \tag{11}$$

Only the slowly varying part $\overline{\varphi}$ is resolved by the Delft3D flow module. In addition, we define the short-wave average of the depth-averaged velocity $\hat{\mathbf{u}}$ and the related fluctuating part $\mathbf{u}''$ as follows:

$$\overline{H\mathbf{u}} = \overline{H}\hat{\mathbf{u}}, \quad \mathbf{u} = \hat{\mathbf{u}} + \mathbf{u}''. \tag{12}$$

This is comparable with the Favre (density-weighted) averaging (Favre (1965)) used in the modeling of compressible turbulent flow. The reason for introducing another short-wave averaging will become clear later. Also for this short-wave average, relations similar to Eqs. (10) and (11) hold:

$$\hat{\hat{\mathbf{u}}} = \hat{\mathbf{u}}, \quad \widehat{\mathbf{u}''} = 0. \tag{13}$$

Application of the previously discussed relations leads to:

$$\begin{aligned}\overline{\mathbf{u}\mathbf{q}} &= \overline{H\mathbf{u}\mathbf{u}} = \overline{H}\widehat{\mathbf{u}\mathbf{u}} = \overline{H}\left(\widehat{\hat{\mathbf{u}}\hat{\mathbf{u}}} + 2\widehat{\hat{\mathbf{u}}\mathbf{u}''} + \widehat{\mathbf{u}''\mathbf{u}''}\right) \\ &\approx \overline{H}\left(\hat{\mathbf{u}}\hat{\mathbf{u}} + 2\widehat{\hat{\mathbf{u}}\mathbf{u}''} + \widehat{\mathbf{u}''\mathbf{u}''}\right).\end{aligned} \tag{14}$$

In the last step, we have used the approximation: $\widehat{\hat{\mathbf{u}}\hat{\mathbf{u}}} \approx \hat{\mathbf{u}}\hat{\mathbf{u}}$. This approximation is valid, since averaging the product of two already averaged quantities can only but yield a quantity very close to the original product.

Taking the short-wave average of Eqs. (1) and (2) yields:

$$\frac{\partial \overline{H}}{\partial t} + \nabla\cdot\overline{\mathbf{q}} = 0, \tag{15}$$

$$\frac{\partial \overline{\mathbf{q}}}{\partial t} + \nabla\cdot(\overline{\mathbf{u}\mathbf{q}}) + \nabla\left(\tfrac{1}{2}g\overline{\tilde{H}^2}\right) - (g\overline{H} + \overline{p_b})\nabla h + \nabla\cdot(\overline{H\boldsymbol{\tau}}) = 0. \tag{16}$$

Rearranging terms in expression (16) and application of Eq. (14) leads to:

$$\begin{aligned}&\frac{\partial \overline{H}\hat{\mathbf{u}}}{\partial t} + \nabla\cdot(\overline{H}\hat{\mathbf{u}}\hat{\mathbf{u}}) + \nabla\left(\tfrac{1}{2}g\overline{H}^2\right) - g\overline{H}\nabla h \\ &= -\nabla\cdot\left(\overline{H}\,\widehat{\mathbf{u}''\mathbf{u}''} + 2\overline{H}\,\widehat{\mathbf{u}''\mathbf{u}''} + \overline{H\boldsymbol{\tau}}\right) + \nabla\left(\tfrac{1}{2}g\left(\overline{H}^2 - \overline{\tilde{H}^2}\right)\right) + \overline{p_b}\nabla h.\end{aligned} \tag{17}$$

This expression is now rewritten into a form that is probably more familiar.

Starting with the time derivative, we get:

$$\frac{\partial \overline{H}\hat{\mathbf{u}}}{\partial t} = \overline{H}\frac{\partial \hat{\mathbf{u}}}{\partial t} + \hat{\mathbf{u}}\frac{\partial \overline{H}}{\partial t} = \overline{H}\frac{\partial \hat{\mathbf{u}}}{\partial t} - \hat{\mathbf{u}}(\nabla\cdot\overline{\mathbf{q}}), \tag{18}$$

where we have used the chain rule in the first, and expression (15) in the second step. The convective term can be rewritten as follows:

$$\nabla\cdot(\overline{H}\hat{\mathbf{u}}\hat{\mathbf{u}}) = \hat{\mathbf{u}}\nabla\cdot(\overline{H}\hat{\mathbf{u}}) + \overline{H}(\hat{\mathbf{u}}\cdot\nabla)\hat{\mathbf{u}} = \hat{\mathbf{u}}\nabla\cdot\overline{\mathbf{q}} + \overline{H}(\hat{\mathbf{u}}\cdot\nabla)\hat{\mathbf{u}}, \tag{19}$$

where, again, we have used the chain rule in the first, and expression (15) in the second step. The last two terms in Eq. (17) can be taken together, giving:

$$\nabla\left(\tfrac{1}{2}g\overline{H}^2\right) - g\overline{H}\nabla h = g\overline{H}\nabla\overline{H} - g\overline{H}\nabla h = g\overline{H}\nabla(h + \overline{\zeta}) - g\overline{H}\nabla h = g\overline{H}\nabla\overline{\zeta}. \tag{20}$$

Inserting Eqs. (18)–(20) into Eq. (17), and division by $\overline{H}$, gives the following, more familiar, form:

$$\frac{\partial \hat{\mathbf{u}}}{\partial t} + (\hat{\mathbf{u}}\cdot\nabla)\hat{\mathbf{u}} + g\nabla\overline{\zeta} = \frac{\mathbf{F}}{\rho\overline{H}}, \tag{21}$$

where

$$\mathbf{F} = -\rho\nabla\cdot\left(\overline{H}\,\widehat{\mathbf{u}''\mathbf{u}''} + 2\overline{H}\,\widehat{\hat{\mathbf{u}}\mathbf{u}''} + \overline{H\boldsymbol{\tau}}\right) + \rho\nabla\left(\tfrac{1}{2}g\left(\overline{H}^2 - \overline{\tilde{H}^2}\right)\right) + \rho\overline{p_b}\nabla h \tag{22}$$

represents the total short-wave induced force. Expression (21) is essentially the nonlinear shallow water momentum equation as implemented in the Delft3D flow module, with total wave force $\mathbf{F}$ (units: $\mathrm{N/m^2}$) driving the current $\hat{\mathbf{u}}$ and causing a change in the mean water level $\overline{\zeta}$. This change in the mean water level is usually called setdown if $\overline{\zeta}<0$, and setup if $\overline{\zeta} > 0$. The wave force is, apart from the sign, identical to the divergence of the radiation stress tensor S: $\mathbf{F} = -\nabla\cdot S$. The wave force needs to be computed in TRITON. However, expression (22) is cumbersome to evaluate directly. Therefore instead, we evaluate the left-hand side of Eq. (21) in TRITON and equate that, after multiplication with $\rho\overline{H}$, to the force. Noise in the total wave-induced force due to local spatial effects, e.g., bathymetry gradients, are smoothed by employing a Shapiro (1970) filter in space. The force is then transferred to the Delft3D flow module. In order to compute the left-hand side of Eq. (21) in TRITON, we need to have available the short-wave averaged components of the dependent variables $\mathbf{u}$ and ζ, i.e. $\hat{\mathbf{u}}$ and $\overline{\zeta}$. In other words, we need a procedure to actually perform the separation as proposed in Eq. (9). This is discussed briefly in the next section.

As a final remark, we note that the reason for introducing quantity $\hat{\mathbf{u}}$ through definition (12) lies in the convenient results, in particular expression (21), that we get through Eqs. (18) and (19). As we saw, application of the continuity equation leads to a cancellation of the term $\hat{\mathbf{u}}(\nabla\cdot\overline{\mathbf{q}})$. If we would have applied separation (9), instead of Eq. (12), to the velocity, such a cancellation would not have occurred. Taking the short-wave average of the depth-integrated velocity according to Eq. (9) then yields:

$$\overline{\mathbf{q}} = \overline{H\mathbf{u}} = \overline{(\overline{H} + H')(\overline{\mathbf{u}} + \mathbf{u}')} = \overline{\overline{H}\overline{\mathbf{u}}} + \overline{H'\overline{\mathbf{u}}} + \overline{\overline{H}\mathbf{u}'} + \overline{H'\mathbf{u}'}, \tag{23}$$

It is not hard to see that pursuing a strategy following from Eq. (23) does not yield convenient expressions similar to Eqs. (18) and (19), and thereby no convenient expression like Eq. (21). In other words, definition (12) is a prerequisite to arrive at a convenient expression.

3.2. Separation of waves into long-wave and short-wave components

The separation of a time signal $\varphi = \varphi(t)$ (e.g., surface elevation) leads to two components: $\varphi' = \varphi'(t)$ is assumed to contain all wave components with a frequency larger than the separation-frequency f_{sep}, and $\overline{\varphi} = \overline{\varphi}(t)$ contains the frequencies smaller than f_{sep}. Here, f_{sep} is a user-defined parameter indicating the separation-frequency between 'short' and 'long' waves, the latter including currents. The employed procedure (with details in Appendix A) consists of recursive application (N_f times, N_f being the filter order) of the low-pass filter:

$$\overline{\varphi}_n = \varepsilon\varphi_n + (1-\varepsilon)\overline{\varphi}_{n-1}, \quad \varepsilon = 2\pi\delta t_T / T_{sep}, \tag{24}$$

where the subscript n denotes the time level, δt_T the TRITON time step, and the separation-time is $T_{sep} = 1/f_{sep}$. It is well known that application of low-pass filters leads to a phase lag. To remedy the phase lag, a delay time between the Delft3D flow and morphology modules on the one hand, and TRITON on the other, is applied. This means that TRITON is running a delay time equal to T_{delay} ahead of the Delft3D modules. A typical value for the delay time for a field case is 10 to 20 s. In Appendix A, the filter procedure and the delay time are discussed in more detail.

Consider now the computation of quantity $\overline{(\varphi')^2}$. Formally, this would require application of low-pass filter (24) two times in sequence: the first one to obtain φ', and the second one, using this φ', to obtain $\overline{(\varphi')^2}$. This implies a delay time twice as large, which destroys accuracy. Another procedure is proposed, in which the low-pass filter is applied only once. Consider the following expression:

$$\overline{\varphi^2} = \overline{(\overline{\varphi} + \varphi')^2} = \overline{(\overline{\varphi})^2} + 2\overline{\overline{\varphi}\varphi'} + \overline{(\varphi')^2}. \tag{25}$$

As already mentioned earlier, averaging the product of two already averaged quantities yields a quantity very close to the original product, hence: $\overline{(\overline{\varphi})^2} \approx (\overline{\varphi})^2$. A similar reasoning leads to: $\overline{\overline{\varphi}\varphi'} \approx \overline{\varphi}\overline{\varphi'} = 0$. Inserting these approximations into Eq. (25) leads to:

$$\overline{(\varphi')^2} \approx \overline{\varphi^2} - (\overline{\varphi})^2. \tag{26}$$

Evaluation of this expression leads to a delay of T_{delay}, since evaluation of $\overline{\varphi^2}$ and $(\overline{\varphi})^2$ both require application of low-pass filter (24) once. The previous discussion provides us with a means to compute time series of the wave height of the short waves:

$$H_{rms,sw} = 2\sqrt{2\overline{(\zeta')^2}} \approx 2\sqrt{2}\sqrt{\overline{\zeta^2} - (\overline{\zeta})^2}. \tag{27}$$

This wave height does not contain the effect of a slow variation in the mean water level due to, e.g., tides. Similarly, the root-mean square orbital velocity follows from:

$$u_{rms,sw} = \sqrt{\overline{(u'')^2}} \approx \sqrt{\overline{u^2} - (\hat{u})^2} \tag{28}$$

The separated velocities are also used in the computation of the following velocity moments, see Roelvink and Stive (1989) and Roelvink and Reniers (1995):

$$guss = \left\langle u''|u''|^2 \right\rangle, \quad guls = 3\left\langle \hat{u}|u''|^2 \right\rangle \tag{29}$$

where $\langle\rangle$ stands for a simple long-term time averaging, and *guss* and *guls* are the third-order wave velocity moments (velocity skewness) in the (short-wave) averaged suspended sediment transport equation due to wave asymmetry (Roelvink and Stive, 1989).

3.3. Roller wave force and organized wave force

In Section 3.1, the computation of the total wave force $\mathbf{F}$ is presented. This force needs to be split into an organized (body) force $\mathbf{F}_w$ and a roller (surface) force $\mathbf{F}_r$:

$$\mathbf{F} = \mathbf{F}_w + \mathbf{F}_r. \tag{30}$$

The motivation for this splitting will become clear in a moment.

The roller concept was introduced by Svendsen (1984a), who defined it as a body of water that moves with the wave in front of the wave crest. The roller is advected with the phase celerity of the wave, thereby exerting a shear stress on the slower moving underlying water mass. This implies that the roller force acts at the water surface and causes the cross-shore circulation of a water mass moving shoreward in the top of the water column and seaward along the bottom (undertow). This also implies that the roller force has to be directed shoreward. We refer to Reniers et al. (2004b) for details.

The organized force stems from the orbital wave motion, and exerts a stress that is assumed to be more or less uniformly distributed over the vertical. This assumption is valid for the near-shore applications considered in the present paper. In deeper water, this assumption is not valid anymore, and one should use the 3D form of the radiation stresses, as pointed out by Ardhuin et al. (2008) and Mellor (2008).

As previously stated, the presence of a roller force leads to the occurrence of undertow, while the organized force acts uniformly over the depth. This explains also why, for morphodynamic computations, it is necessary to have both force components available as separate entities. These components 'drive' the flow in the Delft3D flow model in a different fashion, as will be explained in Section 4.1.

Note that the computed wavefield, the total wave-induced force $\mathbf{F}$ and the associated change in mean water level $\overline{\zeta}$ (setdown or setup) do not depend on the splitting in Eq. (30).

The next step is to derive an expression, in time domain, for the roller force. The roller energy E_r, i.e. the kinetic energy of the roller per unit area, is related to the roller area A_r by means of (Svendsen (1984a)):

$$E_r = \frac{1}{2}\rho c^2 \frac{A_r}{L}, \tag{31}$$

with L a representative value for the wave length and c the phase celerity. The roller area A_r is defined as:

$$A_r = \int_0^L \delta(s) ds, \tag{32}$$

where $\delta = \delta(s)$ is the roller thickness of the turbulent wedge as a function of coordinate s (in direction of the roller). Assuming that the roller is steady and is propagating with celerity c, Svendsen (1984a) states that:

$$A_r \approx c \int_0^T \delta(t) dt, \tag{33}$$

where $\overline{\delta}$ is the wave-averaged roller thickness and T a representative value for the wave period. Writing out yields:

$$c\int_0^T \delta(t)dt = cT \cdot \frac{1}{T}\int_0^T \delta(t)dt = cT\overline{\delta} = L\overline{\delta}. \tag{34}$$

The roller dissipation is given by (Reniers et al., 2004a):

$$D_r = \frac{2g \sin\beta E_r}{c}, \tag{35}$$

where β is the roller angle. Restricting ourselves to 1D, the roller force is expressed following Nairn et al. (1990) and Reniers (1999) as

$$F_r = \frac{D_r}{c}. \tag{36}$$

Combining the previously discussed expressions yields:

$$F_r = \rho g \sin\beta \cdot \overline{\delta}. \tag{37}$$

Once the total wave force (expression (22)) and the roller force (expression (37)) are available, the organized wave force follows from, cf. Eq. (30): $\mathbf{F}_w = \mathbf{F} - \mathbf{F}_r$.

From numerical experiments it turns out that putting simply $\delta = \delta^*$ does not yield accurate answers. Therefore, another closure hypothesis is needed to relate the roller thickness δ, which represents the thickness of the turbulent wedge of the roller (a physically real quantity), to the roller thickness δ^* as computed in the TRITON breaking model (a numerical quantity). Two closure hypotheses will be considered in this paper.

Closure hypothesis 1. Linear relation between δ and δ^*

A linear relation is assumed between δ and δ^*:

$$\delta = f_\delta \delta^*. \tag{38}$$

This is sketched in Fig. 2.

Obviously, this implies $\overline{\delta} = f_\delta \overline{\delta^*}$. Combining the expressions (37) and (38) yields:

$$F_r = \rho g \sin\beta \cdot f_\delta \overline{\delta}^*, \tag{39}$$

i.e. the roller force is proportional to the roller thickness as computed by the TRITON wave breaking model. For $f_\delta > 1$, the thickness of the turbulent wedge is thicker than the roller thickness, which is represented by the distance between the straight line and the free surface in Fig. 2.

Closure hypothesis 2. Breaker delay

The idea behind the TRITON wave breaking model is that wave dissipation only occurs when waves are steeper than a given threshold, i.e. when the computed roller thickness δ^* is larger than zero. Similarly, when the computed roller thickness is zero, no wave dissipation is assumed to take place. Propagating shoreward, wave dissipation and the turbulence due to breaking are assumed to start at roughly the initial wave-breaking location, e.g., a bar. However, once the wave dissipation process is finished, for example in a trough after the bar or very close to the shoreline, with virtually zero wave height, the turbulent wedge of the physical roller continues for some time to slide over the underlying water mass. This implies that the turbulent wedge continues to exist and to propagate shoreward after the 'computed' roller has ceased to exist. We will refer to this effect as breaker delay. As a side-note we remark that this is not related, at least not directly, to the following phenomenon identified by Nairn et al. (1990): the rollers of breaking waves are responsible for a spatial lag between the position where wave breaking is initiated and the position where wave set-up increases largely. In our approach, the spatial lag between wave breaking and wave set-up is included in the TRITON model equations and does not need additional modeling.

The effect of breaker delay can be seen in measurement data, such as Fig. 3.5 in Boers (2005), which is reproduced here in Fig. 3. This figure suggests a relation between the observed wave energy dissipation (D_b) and the observed fraction of waves with a roller (Q_r). Both quantities demonstrate a strong increase at the beginning of the wave breaking process. The observed fraction of waves with a roller (thought to correspond with $\delta > 0$) in the middle panel reaches its maximum at a location which is more shoreward than the location where dissipation (thought to be correspond with $\delta^* > 0$), shown in the upper panel, is maximal.

The easiest way to obtain a relation between the physical roller thickness $\delta = \delta(x)$ and the computed roller thickness $\delta^* = \delta^*(x)$ satisfying the aforementioned requirements is by applying a seawards averaging of the following form:

$$\delta(x) = f_\delta \frac{1}{L_{delay}} \int_{x-L_{delay}}^{x} \delta^*(s) ds. \tag{40}$$

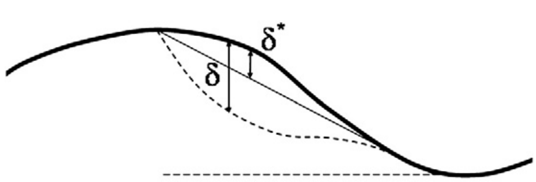

Fig. 2. Hypothesis 1. Linear relation between the thickness of the turbulent wedge (δ) and the roller thickness as computed in TRITON (δ^*).

Note that the positive x-direction points shoreward and that we have added a tunable constant f_δ. Quantity L_{delay} represents a measure for the length over which the averaging ('delay') takes place. A value for this quantity must be derived from observational data. Our numerical experiments, to be described in Section 5, led to the following suitable value for L_{delay}:

$$L_{delay}(x) = c(x) T_{sw} = \sqrt{gh(x)}\, T_{sw}, \tag{41}$$

where T_{sw} is a representative value for the short-wave period at the wave boundary. Short-wave averaging of the result obtained from Eq. (40) yields $\overline{\delta}$, which can be inserted in Eq. (37).

Note that it is possible to estimate the roller force from experimental data; see Appendix B for the procedure for this. This will be used to validate the closure hypotheses, as will be done in Sections 5.2 and 5.3.

3.4. Summary

Here we briefly summarize the findings so far. Short-wave averaging of the TRITON momentum equation yields an expression for the total wave force **F**. This force is evaluated in TRITON and transferred to the Delft3D flow module, where it is used to obtain the wave setdown/setup, cf. expression (21). Also in TRITON, the wave force is split into an organized (body) force and a roller (surface) force, see Eq. (30). The organized wave force acts over the total water column. The roller force acts on the water surface and causes a velocity undertow profile. This has, being especially large in the breaker zone, a significant impact on sediment transport. Based on existing expressions, the time-domain expression (37) for the roller force is derived. Two different closure hypotheses for the evaluation of the roller force, expressions (38), (40) and (41), will be investigated in this paper. The roller force is computed in TRITON, and is transferred to Delft3D flow module.

4. Flow and sediment transport model

In this section, the flow and morphology modules of Delft3D are described, in Sections 4.1 and 4.2. In Section 4.3, the coupling between TRITON and Delft3D is discussed.

4.1. Flow model

The Delft3D flow module (Stelling, 1983; Lesser et al., 2004) is based on the hydrostatic flow assumption and solves the short-wave averaged 3D shallow water equations. The model is capable of predicting infra-wave aspects (e.g. currents and long waves), but not intra-wave aspects (e.g. short waves). As discussed previously, intra-wave effects such as wave setdown/setup and undertow can be taken into account by providing the flow module with the wave forces. The organized wave force acts uniformly over the vertical, while the roller force acts at the surface; see Walstra et al. (2000) for details on the implementation in the flow module. An obvious consequence is that it is necessary to have vertical resolution in the flow model; this is the only way in which, for example, undertow can be modelled correctly.

4.2. Sediment transport model

Sediment transport consists of three components: bed-load transport, current-related suspended load transport and wave-related suspended load transport.

To evaluate the current-related sediment transport, an advection diffusion equation for the suspended sediment transport is computed in the Delft3D morphology module, with hydrodynamic input from

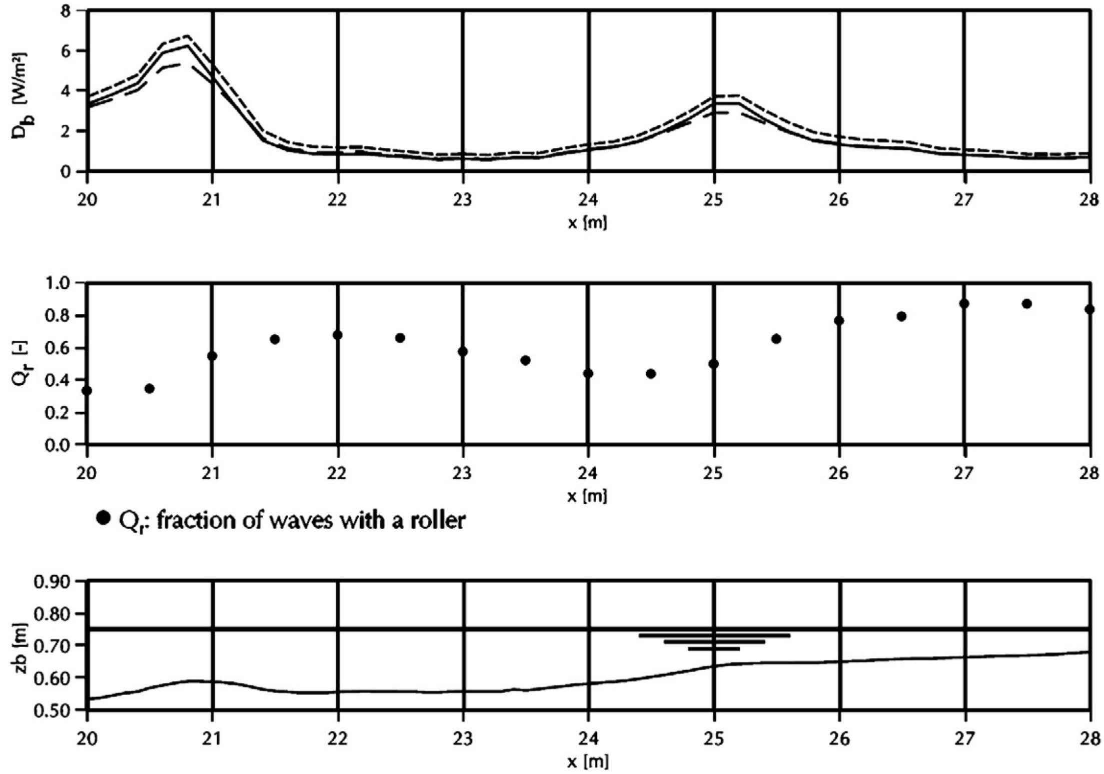

Fig. 3. Wave energy dissipation (D_b) as computed by different models (upper panel); observed fraction of waves with a roller (Q_r) (middle panel); employed bathymetry (lower panel). Reproduced from and with permission of Boers (2005), Fig. 3.5.

the Delft3D flow module. This is described in detail in Lesser et al. (2004).

The wave-related suspended transport only occurs due to wave asymmetry effects in coastal region. In Van Rijn et al. (2004), the following approximation method for wave-related suspended sediment transport is proposed:

$$S_{s,w} = f_{SUSW}\gamma U_A L_T \tag{42}$$

where f_{SUSW} is a user specified tuning parameter set to 0.85 and γ is a phase lag coefficient set to 0.1. The approximated suspended sediment load is given by $L_T = 0.007\rho_s d_{50} M_e$, where ρ_s is the sediment density, d_{50} the median particle diameter, and M_e the excess sediment mobility number due to waves and currents:

$$M_e = \frac{\rho\left(v_{eff} - v_{cr}\right)^2}{(\rho_s - \rho)gd_{50}}, \quad v_{eff} = \sqrt{v_R^2 + U_{\delta,for}^2}. \tag{43}$$

Here, v_{cr} is the critical depth averaged velocity for initiation of motions (based on a parameterisation of the Shields curve), and v_R is the magnitude of an equivalent depth-averaged velocity computed from the velocity in the bottom computational layer, assuming a logarithmic profile. The term $U_{\delta,for}$ will be explained later. The effect of wave asymmetry is modeled in Van Rijn et al. (2004) as:

$$U_A = \frac{U_{\delta,for}^4 - U_{\delta,back}^4}{U_{\delta,for}^3 + U_{\delta,back}^3} \tag{44}$$

where $U_{\delta,for}$ and $U_{\delta,back}$ are the near bed peak orbital velocity (m/s) in the onshore direction (wave direction) respectively offshore direction (against wave direction) based on Stokes and cnoidal wave theory. In the present paper, another formulation for the term formed by the product of the wave asymmetry and the phase lag is proposed:

$$\gamma U_A = \frac{\overline{u_b''(t)\left|u_b''\left(t - t_{lag}\right)\right|^3}}{\overline{\left|u_b''\left(t - t_{lag}\right)\right|^3}}. \tag{45}$$

Here, t_{lag} is the time lag, put to 1 s, between the saltation of the sediment particles and them being carried away. This term has a similar purpose as the phase lag coefficient γ. Evaluation of Eq. (45) is done in TRITON, using the bottom orbital velocities and application of the separation procedure as described in Section 3.2. In other words, the wave asymmetry is computed using intra-wave time series (instead of being based on parameterization), transferred to Delft3D and incorporated there in the sediment transport formulas.

The bed-load transport can be computed in the Delft3D morphology module, employing parameterized intra-wave properties. However, it is also possible to perform the bed-load transport computations in TRITON. The latter is opted for, since it has the advantage of avoiding parameterization of the short waves. The bed-load transport formulation of Van Rijn et al. (2004) has been implemented in TRITON. For the validation cases described in this paper, it turned out that the effect of bed-load transport is significantly smaller than that of the other two components. Following Rakha et al. (1997), we have not included bed-load transport in the simulations described in this paper.

4.3. Set up of simultaneous simulations

As stated previously, the 2DH Boussinesq-type wave model TRITON and the Delft3D flow and morphology modules are coupled online, which means that they run in parallel, while exchanging updated information (see Fig. 4). The coupling between the Delft3D flow and morphology modules, briefly referred to as the Delft3D model, is discussed in Lesser et al. (2004), and will not be treated in the present paper.

TRITON uses a time step Δt_T and a gridcell size δx_T with typical dimensions $T_{sw}/30$ and $L_{sw}/30$ (or smaller) respectively, where T_{sw} and L_{sw} represent typical values for the short-wave period and wave length respectively. The Delft3D model is computing the long waves with a time step Δt_{D3D} and a gridcell size Δx_{D3D}. Typical values for the ratios $\Delta t_{D3D} / \Delta t_T$ and $\Delta x_{D3D} / \Delta x_T$ range between 5 and 20. As a consequence of the wave separation procedure, see Section 3.2, TRITON runs a time lapse equal to T_{delay} ahead of the Delft3D model.

At every Delft3D time step and gridpoint, the following data is transferred from TRITON to the Delft3D model: the bedload transport, the total wave-induced force $\mathbf{F}$, the roller force $\mathbf{F}_r$, the wave asymmetry γU_A term as needed for the suspended sediment transport, the short-wave averaged wave height $H_{rms,sw}$, the short-wave averaged orbital velocities $u_{rms,sw}$ and $v_{rms,sw}$, the roller dissipation D_r, the mass flux of the roller M_r, and the wave direction. The following data is transferred from the Delft3D model to TRITON: the updated bathymetry, including the tide update (see Section 5.4).

5. Validation

The coupled Delft3D-TRITON model is validated against a number of cases from laboratory flume experiments (LIP and Boers) and field measurements (Duck94). In Section 5.1, a description of the LIP and Boers experiments is given. Validation for the cases LIP-1C and Boers-1C is discussed in Section 5.2. Section 5.3 is devoted to validation cases LIP-1B and Boers-1B. Validation of the model for an onshore bar movement observed in September 1994 at the field measurement site Duck forms the topic of Section 5.4. The model settings are given in Appendix C.

5.1. Model settings for model-data comparisons

In 1993, the LIP11D experiments were carried out in the Delft Hydraulics' Delta Flume with the purpose of obtaining detailed experimental data of hydrodynamics and sediment transport in a barred surf zone with irregular waves (Arcilla et al. (1994), Roelvink and Reniers (1995)). Experiments were also conducted in the Wave Flume of the Fluid Mechanics Laboratory of the Delft University of Technology, see Boers (1996) and Boers (2005). The experiments performed by Boers are considered as a follow-up of the LIP11D experiments, since the studied bathymetry and wave conditions are very similar. The differences between the LIP11D and the Boers experiments are threefold: the latter are performed on a reduced scale (roughly a factor 6 reduction in flume dimensions and wave conditions) and on a concrete, therefore non-eroding bottom. The experiments by Boers also yielded high-resolution data, including surface elevation measurements (70 locations) and vertical velocity profiles (28 locations, with typically 10 data points distributed over the depth, per location).

The layout of the LIP experiment and the bathymetry of the Boers experiment are shown in Fig. 5 (the wave board is to the left). As the red line in Fig. 5B shows, the bed profile is truncated in the TRITON simulation at small water depths to avoid drying and flooding, whereas the black line is the bathymetry as used in the Boers experiments.

Erosive (1B) and accretive (1C) wave conditions for the Boers and LIP experiments are studied in this paper, see Table 1. For morphological validation, we will compare with the results of the first six wave hours of LIP-1B and LIP-1C.

5.2. Validation case 1C

5.2.1. Boers

Case 1C is a slightly accretive condition, where the bar moves shoreward. Model-data comparisons for Boers-1C are shown in Fig. 6. Up to the bar, TRITON slightly over-predicts the wave height (Fig. 6A). However, from the bar on shoreward, the wave height prediction is good, including the details of reshoaling. For the wave setdown/setup (Fig. 6B), a similar observation holds: some difference up to the bar, but from the bar on shoreward a good agreement. In addition, the variance density spectra (Fig. 6C) at various locations show a very good agreement. The computed total wave-induced force is, together with its constituents (organized and roller force), shown in Fig. 6D.

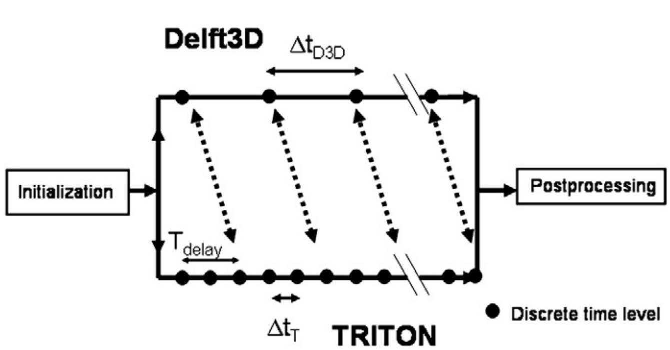

Fig. 4. Flow diagram of the coupling between Delft3D and TRITON.

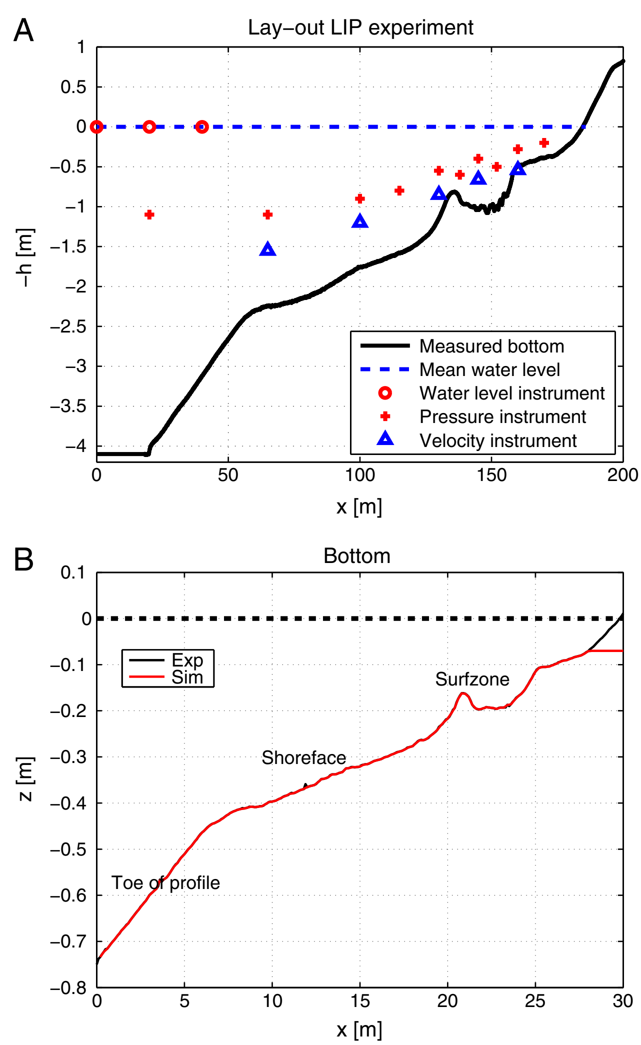

Fig. 5. (A) Lay-out of the LIP experiment, and (B) bathymetry in the Boers experiment.

Table 1
Measured wave parameters in the flume near the waveboard.

Wave test	H_{m0} [m]	T_p [s]
Boers-1B	0.207	2.07
LIP-1B	1.3	5.0
Boers-1C	0.104	3.47
LIP-1C	0.58	8.0

The roller force in this figure is computed using the breaker delay hypothesis and parameter f_δ equal to 2.5.

The two closure hypotheses for the roller force and some suitable values for f_δ are now studied in more detail. This is done by comparing the computed roller force with the roller force as derived from experimental data (see Appendix B for a procedure to do this), and by comparing the computed and measured undertow profiles. Application of the linear relation hypothesis and a value of $f_\delta = 2.5$ lead to a premature (too much seaward) rise of the roller force, and thus undertow (Fig. 7A and B). This can be remedied somewhat by application of a breaker delay ($f_\delta = 2.5$) to get some shoreward shifting of the roller force and therefore of the undertow (Fig. 7C and D). In the trough region (x-values between 22 m and 25 m), the computed amount of undertow is somewhat too small. Increasing the value of f_δ to 7.5 (Fig. 7E and F) leads to an improvement in the trough region, but to an overestimation in the other regions (x-values between 17 m and 22 m, and between 24.8 m and 26 m). Summarizing, an acceptable agreement for the roller force is reached with the breaker delay hypothesis and $f_\delta = 2.5$ (Fig. 7C and D).

5.2.2. Delta Flume

The next step is to include morphology in the computation, that is, to simulate LIP-1C as conducted in the Delta Flume. The roller force is computed using the aforementioned settings. Fig. 8 shows the model-data comparison for LIP-1C for the first six wave hours. Fig. 8A shows the wave height transformation. The maximum peak at $x = 135$ m (just before breaking) as predicted by the model may seem to be a spurious feature. However, a similar peak was measured by Boers, see the black line in Fig. 6A. Fig. 8B shows the measured and predicted undertow profiles in a number of cross-shore locations. In general, the profiles are well predicted offshore of the breakpoint but show an over-prediction in the bar area (between 130 m and 138 m), which will result in a critically higher offshore-directed sediment transport prediction. The most likely reason for this is the fact that wave breaking in the tests took place shoreward of the bar rather than on the crest and on the offshore slope. This behaviour, typical for plunging breakers, is not captured accurately in Boussinesq-type wave models, due to limitations of the wave breaking model.

Fig. 8C shows the measured and predicted concentration profiles in various cross-shore locations. Here also the model overpredicts the sediment concentration. The overprediction is at least partly due to the overestimation of the undertow. An additional simulation (figures not shown in this paper) in which the parameter f_δ is reduced leads to a reduction (underestimation) of the undertow and a reduction of the sediment concentration. The sediment concentration, though reduced, is still too large. Also for the overestimation offshore of the bar no explanation has been found yet. Fig. 8D shows the indirectly measured total sediment transports ("indirectly" because they were calculated on the basis of measured bottom changes) (black line), the

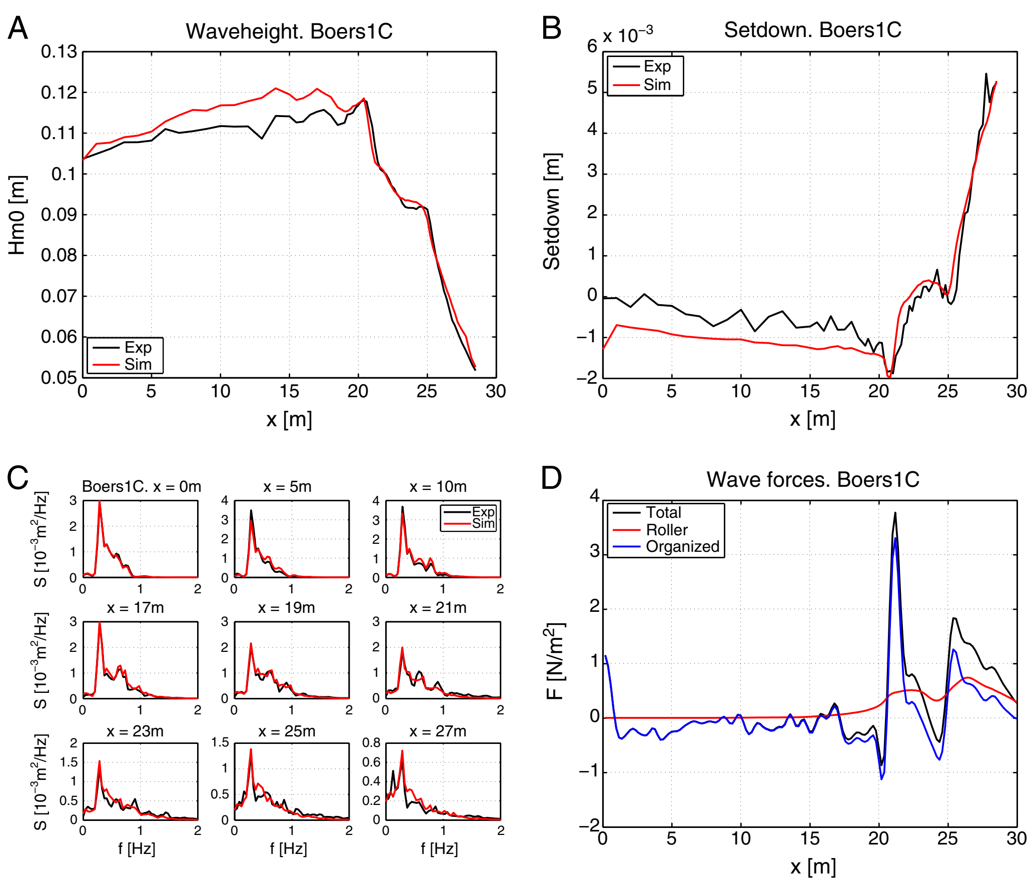

Fig. 6. Model-data comparison for Boers-1C. Red lines are model results and the black lines are experimental data: (A) wave height transformation; (B) wave setdown/setup; (C) variance density spectra at various locations. In (D): the computed wave-induced force (black line), made up of a roller force (red line) and organized force (blue line).

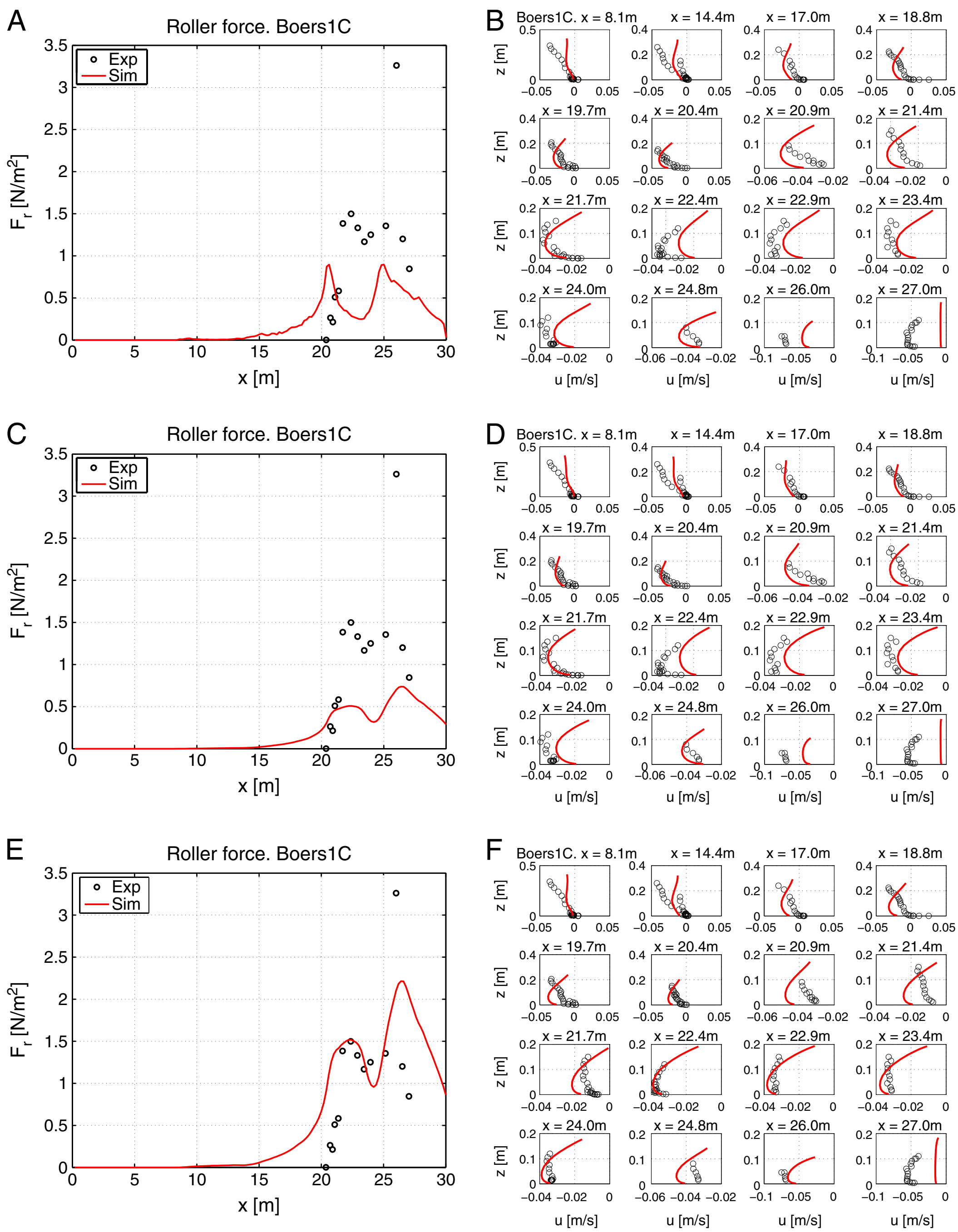

Fig. 7. Roller force and velocity profiles. Red lines are model results and circles are experimental data: (A) and (B) linear relation hypothesis and $f_\delta = 2.5$; (C) and (D) breaker delay hypothesis and $f_\delta = 2.5$; (E) and (F) breaker delay hypothesis and $f_\delta = 7.5$.

model predicted total sediment transport (red line), and its component parts: the wave-related suspended sediment transport (green line) and the current-related suspended sediment transport (blue line).

The model predicts the measurements fairly well, especially up to the peak at breaking, but it does not predict the sediment transport gradient after breaking. This is because the wave-related sediment transport should have decreased more sharply and to a lower level, which is also evident in the over-prediction of the *guss* parameter (in Fig. 8E) immediately after the breaking location. It should be emphasized that, in this validation case, the largest contribution to the bathymetric changes are due to the wave-related suspended sediment transport. This quantity is directly related to the velocity skewness, as is evident from the *guss* parameter. This is consistent with similar recent studies (Lescinski and Özkan-Haller, 2004; Ruessink et al., 2007) in that the predicted onshore-directed sediment transport just offshore of, and in the wave breaking region, is directly related to wave asymmetry.

Finally, a close-up of the bathymetric evolution in the bar-trough region is shown in Fig. 8F. From the same initial bathymetry (green line), both the model and the measurements show a shoreward movement, albeit that the model underpredicts the rate of movement and flattens out the shoreward slope of the bar. This is due to the flatter gradient in the modeled sediment transports, which will cause a migration and diffusion of the bar. However, the model does produce the correct migration direction, which is an improvement over the predictions by Rakha et al. (1997), who showed no bar migration, and by Long et al. (2006), who showed minimal onshore directed transport. However, the Brier skill score computed over the bar region, defined between 120 m and 150 m, yields a skill of $M=0.20$, which is 'poor' according to Van Rijn et al. (2003).

5.3. Validation case 1B

5.3.1. Boers

Case 1B is a highly erosive case, with waves already breaking strongly near the wave board and continuing to break through the entire flume. Model-data comparisons for Boers-1B are shown in Fig. 9. Up to the bar, TRITON slightly underpredicts the wave height, as one sees in Fig. 9A. Behind the bar, this situation is reversed. The variance density spectra (Fig. 9B) show good agreement offshore of the bar; shoreward of the bar there is less agreement. The wave setdown/setup, see Fig. 9C, is accurately predicted. For $f_\delta=7.5$, a reasonable agreement for the undertow profiles is obtained for the breaker delay closure hypothesis (Fig. 9D).

5.3.2. Delta Flume

The next step is to include morphology in the computation, that is, to simulate LIP-1B. Fig. 10 shows the computed results as compared to the validation data for LIP-1B for six wave hours. The wave height prediction (Fig. 10A) shows an underestimation seaward of the bar, and good correspondence from the bar on shoreward. The third-order

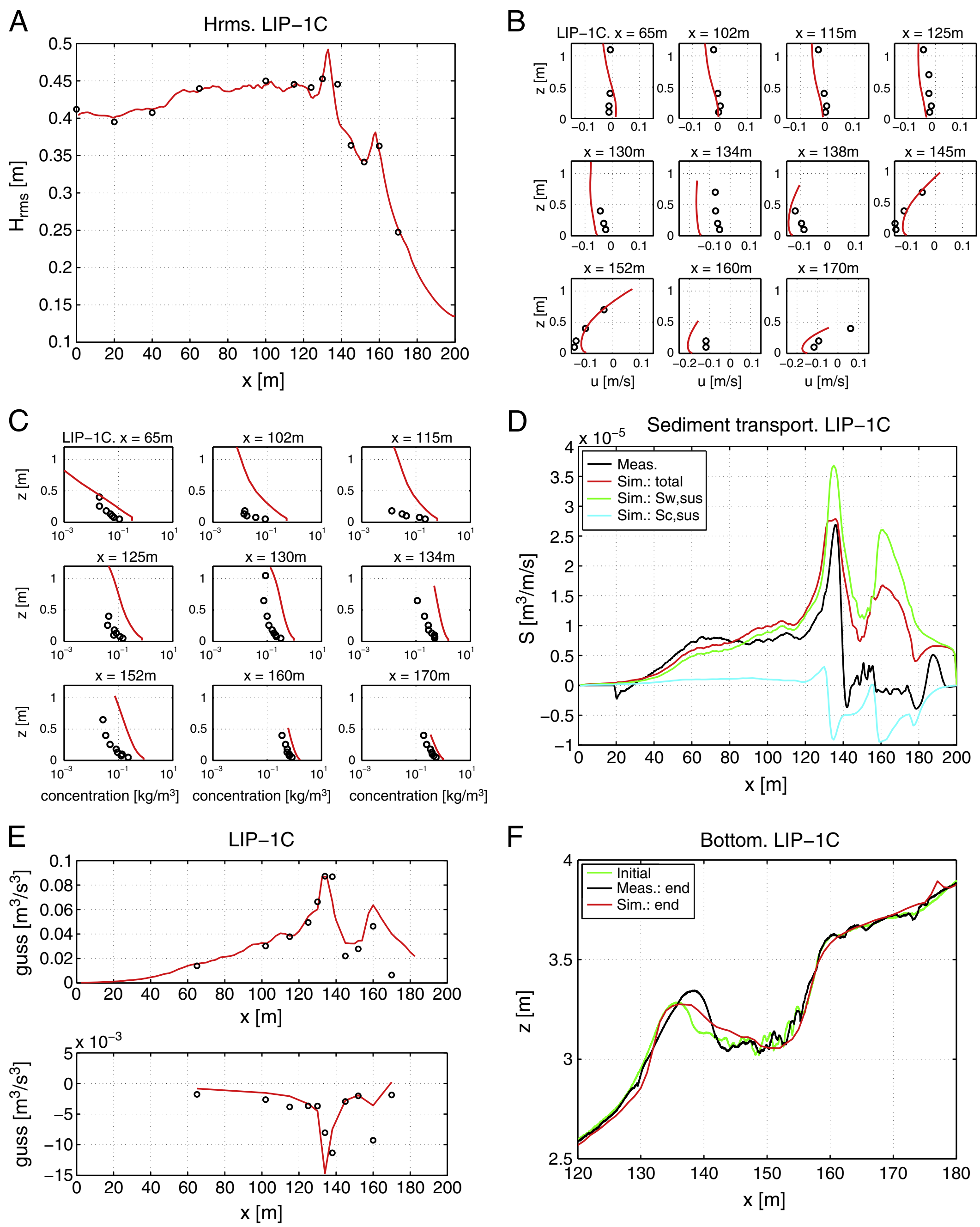

Fig. 8. Model-data comparison for LIP-1C. Red lines are model results and circles are experimental data: (A) wave height transformation; (B) velocity profiles at various locations; (C) sediment concentration at various locations. In (D), measured sediment transport (black line), computed total (red line), computed current-related part (blue line) and computed wave-related part (green line); (E) wave velocity moments; (F) initial bathymetry (green line), measured bathymetry after 6 h (black line) and computed bathymetry (red line).

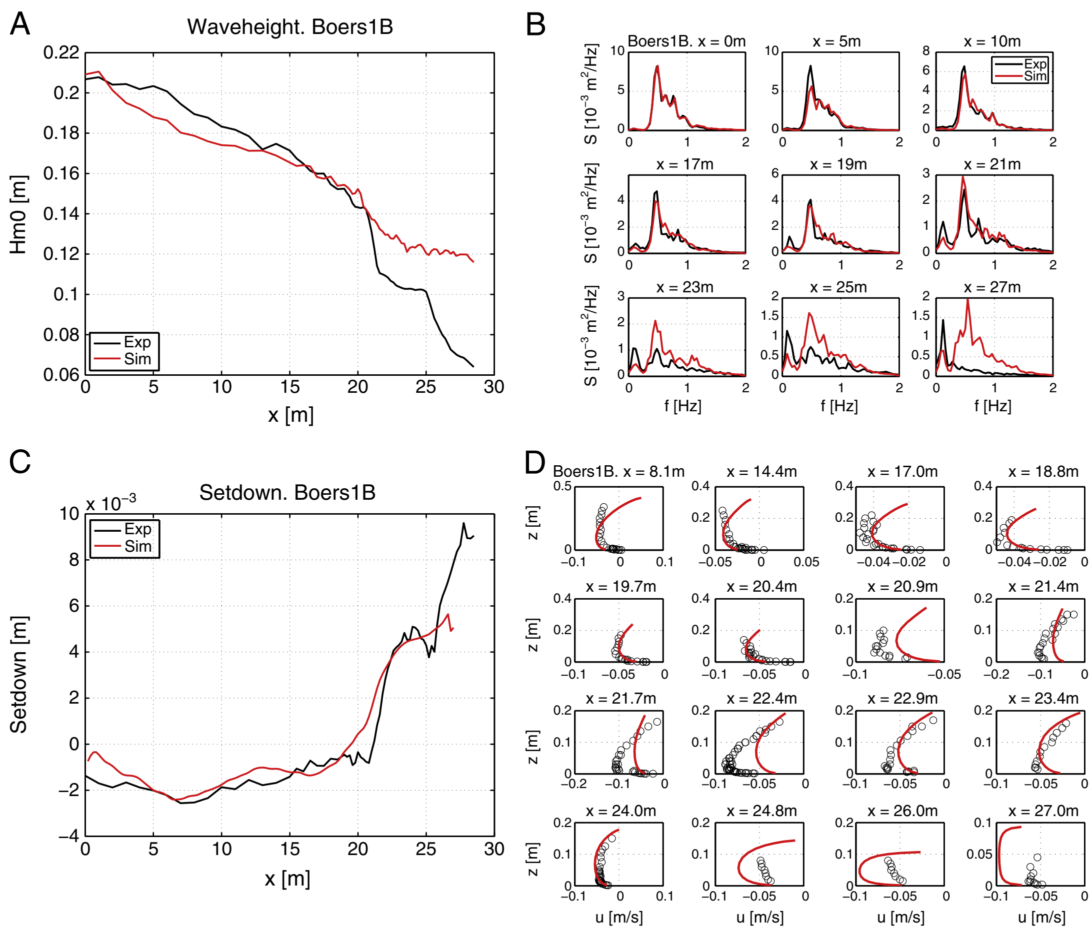

Fig. 9. Model-data comparison for Boers-1B. Red lines are the model results, and the black lines are experimental data: (A) wave height transformation; (B) variance density spectra at various locations; (C) wave setdown/setup. In (D), velocity profiles at various locations: lines are model results, and circles are experimental data.

velocity moments *guss* and *guls* are, given the scatter in the measurements (due to the fact that they were taken from a sled which moved slowly onshore and offshore over the evolving bathymetry), well predicted (Fig. 10B). Also the computed undertow profiles, with the roller force obtained using the breaker delay hypothesis and $f_\delta = 7.5$, and concentration profiles show a good agreement with experimental data (Fig. 10C and D). The total predicted sediment transport (Fig. 10E, red line) does not match the measurements (black line) in magnitude, but predicts the shape in that the gradients are similar. These gradients in the sediment transport are critical for the direction of the bar movement. The figure shows that negative gradients in the sediment transport (inducing accretion) appear seaward of the bar and positive gradients (inducing erosion) appear shoreward of the bar. The location of the gradients is determined by the cross-shore variation of the current-related suspended sediment transport (blue line), which is more important in this case than in LIP-1C. The net result of the erosion and accretion is a seaward movement of the bar, which was both predicted and measured, see Fig. 10F. The Brier skill score computed over the bar region, defined between 120 m and 150 m, yields a skill of $M = 0.39$which is 'reasonable/fair' according to Van Rijn et al. (2003).

5.4. Validation case Duck94

During the Duck94 field experiment conducted near Duck, North Carolina on a barrier island exposed to the Atlantic Ocean, various onshore bar movements were observed (Gallagher et al. (1998)). The onshore bar movement of about 20 m as observed during the period 22–27 September 1994 is taken as validation experiment for the proposed model, with model settings as given in Appendix C. This time period was characterized by a mildly energetic wave climate, with significant wave heights ranging between 0.5 m and 1 m, and a peak wave period floating around 8.5 s (in 8 m of water depth). This particular case has, as mentioned in the introduction section, been studied by various authors. The used data sets are downloaded from the Duck94 webserver. We used bottom data along a ray that extends from about 100 m to 400 m offshore, at a longshore position (Duck FRF coordinate system) of about 930 m. As offshore wave boundary condition, measured time series of the surface elevation from the measurement location at about 400 m offshore is used. Wave data from the SPUVT (Sonar altimeters (S), Pressure gages (P), bi-directional current meters (UV), and Thermistors (T)) dataset is used for validation.

A morphological acceleration factor of 20, see Reniers et al. (2004a), is employed to speed up the computations. Application of a morphological factor in combination with a time-domain phase-resolving model leads to two issues that should be treated with care. The first issues concerns the specification of the TRITON offshore boundary conditions. Fig. 11 shows an example excerpt from the measured water surface elevation signal at $x = 398$ m (FRF coordinate system), where the TRITON offshore boundary is positioned. The red portion of the time series (before the vertical dashed line) is 1/20th the length of the shown signal. A series of these excerpts are taken from the total measured signal, and then put together to produce an input water surface elevation time signal that spans the 22–27 September period, but is 1/20th the length of the measured signal. The

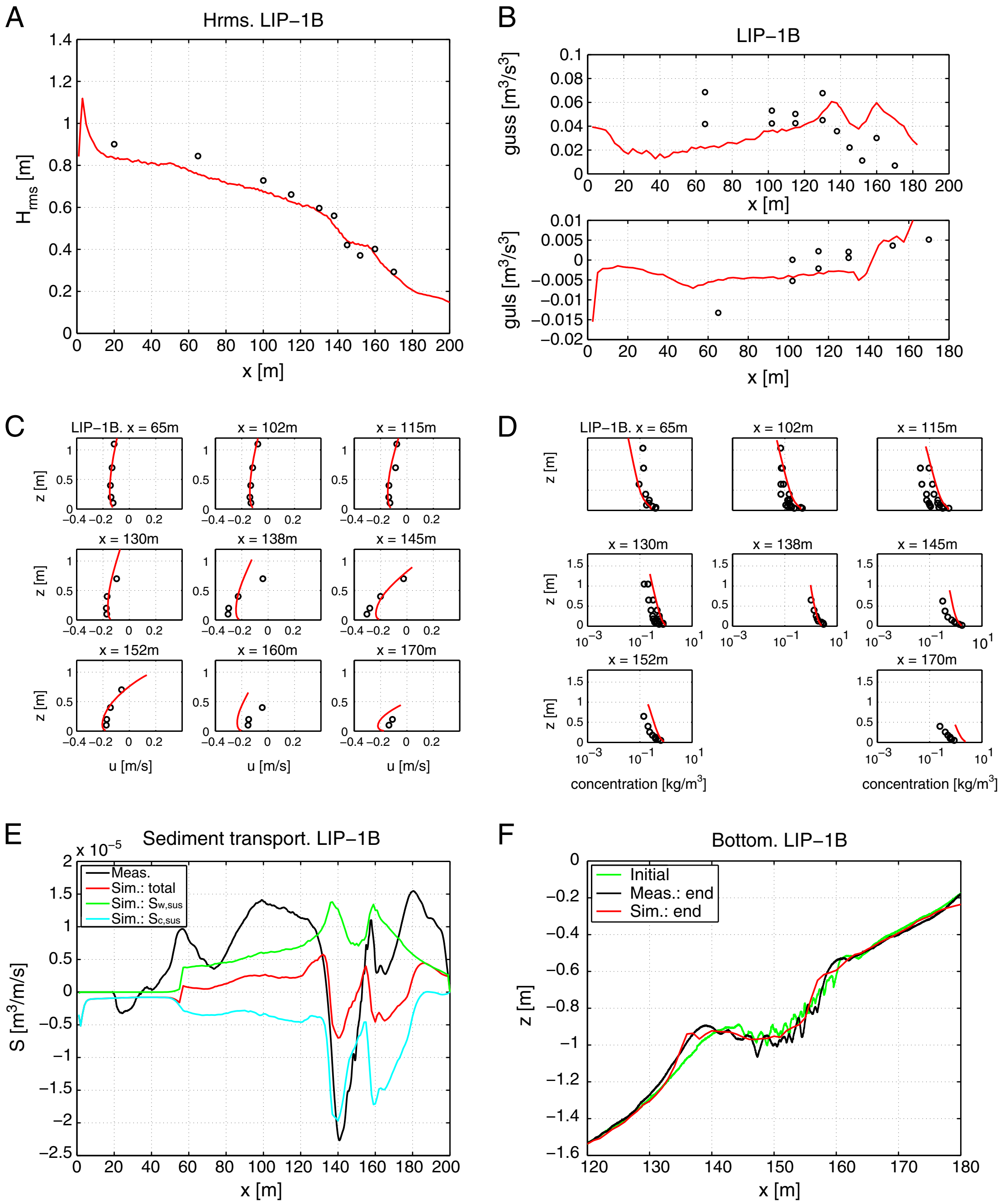

Fig. 10. Model-data comparison for LIP-1B. Red lines are the model results, and the circles are experimental data: (A) wave height transformation; (B) wave velocity moments; (C) velocity profiles at various locations; (D) sediment concentration at various locations. In (E), measured sediment transport (black line), computed total (red line), computed current-related part (blue line) and computed wave-related part (green line); (F) initial bathymetry (green line), measured bathymetry after 6 h (black line) and computed bathymetry (red line).

wave parameters do not change significantly over each portion, so it is expected that taking excerpts instead of the total signal does not have a significant effect on the final results. After having studied various values for the morphological factor, a value of 20 was found to be a satisfactory compromise between computational efficiency and loss of temporal resolution.

The second issue to be treated with care concerns the tidal forcing in combination with a morphological acceleration factor. If the tide were included in the offshore water surface elevation signal, this would result in artificially large (roughly 20 times larger) tidal velocities entering and leaving the domain. On the other hand, omitting tides from the computations is not correct either, since tidal variations in the water level have a significant effect on the wave field. Therefore, the tidal contribution to the total water surface elevation is absorbed into the bathymetry updates (i.e. new bathymetry = old bathymetry + bed change + change in tide elevation). The updated bathymetry computed in Delft3D at every time step, including the tidal contribution, is then passed back to TRITON.

The measured and computed wave parameters wave height and mean wave period (T_{m02}), obtained by a three hour averaging, are shown in Fig. 12A and B for each observational cross-shore location. The wave height is predicted well in the bar-region ($x = 240.55$ m and 264.7 m) throughout the simulation, with an over-prediction of the offshore wave height near the end of the simulation ($x = 295$ m and greater). Onshore of the sand bar region, the model consistently over-predicts the wave height compared to the observations. This is a result

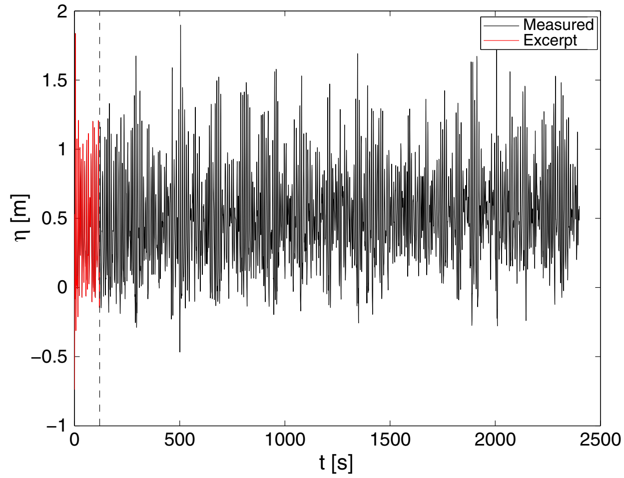

Fig. 11. Water surface elevation excerpt (red; before the vertical dashed line) from the measured signal at $x = 398$ m (FRF coordinates). (For interpretation of the references to color in this figure legend, the reader is referred to the web version of this article.)

of the TRITON wave-breaking model. The mean wave period is consistently under-predicted by TRITON in the region of the sand bar and offshore. Onshore of the sand bar, the model appears to capture some of the wave period behaviour, but does not predict the oscillatory behaviour in time. This may be due to the procedure of taking excerpts to specify the offshore boundary conditions.

The TRITON-Delft3D model predicts onshore-directed movement of the sandbar over the course of the 5-days that has a similar pattern to the observed morphological evolution (Fig. 12C and D). However, the TRITON-Delft3D model predicts the location of the bar crest observed on September 22nd, 19:00 h (beginning of the simulation) at $x = 240.55$ m to maintain its height over the 5-day migration, whereas the bar was observed to grow in height at this location. The TRITON-Delft3D model is able to predict the erosion of the offshore flank of the sand bar ($x = 260$ m–300 m) and the growth of a new bar crest shoreward of the original crest. The extent of the onshore migration of sediment is slightly over-predicted and the shape of the new sand bar region is not accurately predicted, but we are successful at predicting the location of the new bar crest. The Brier skill score computed over the bar region, defined between 165 m and 350 m, yields a skill of $M = 0.42$, which is 'reasonable/fair' according to Van Rijn et al. (2003).

5.5. Summary of results

Assessment of skill of these tests was done using the following set of error parameters, see also Roelvink et al. (2009) and Sutherland et al. (2004) (Table 2).

The statistical scores for each of the test cases, according to the definitions of the scores in Table 3 is given and shows that the model performs well for the diversity of tests.

6. Conclusions

The present paper discusses the online coupling of hydrodynamic models for waves (TRITON) and flow (Delft3D flow module) with a

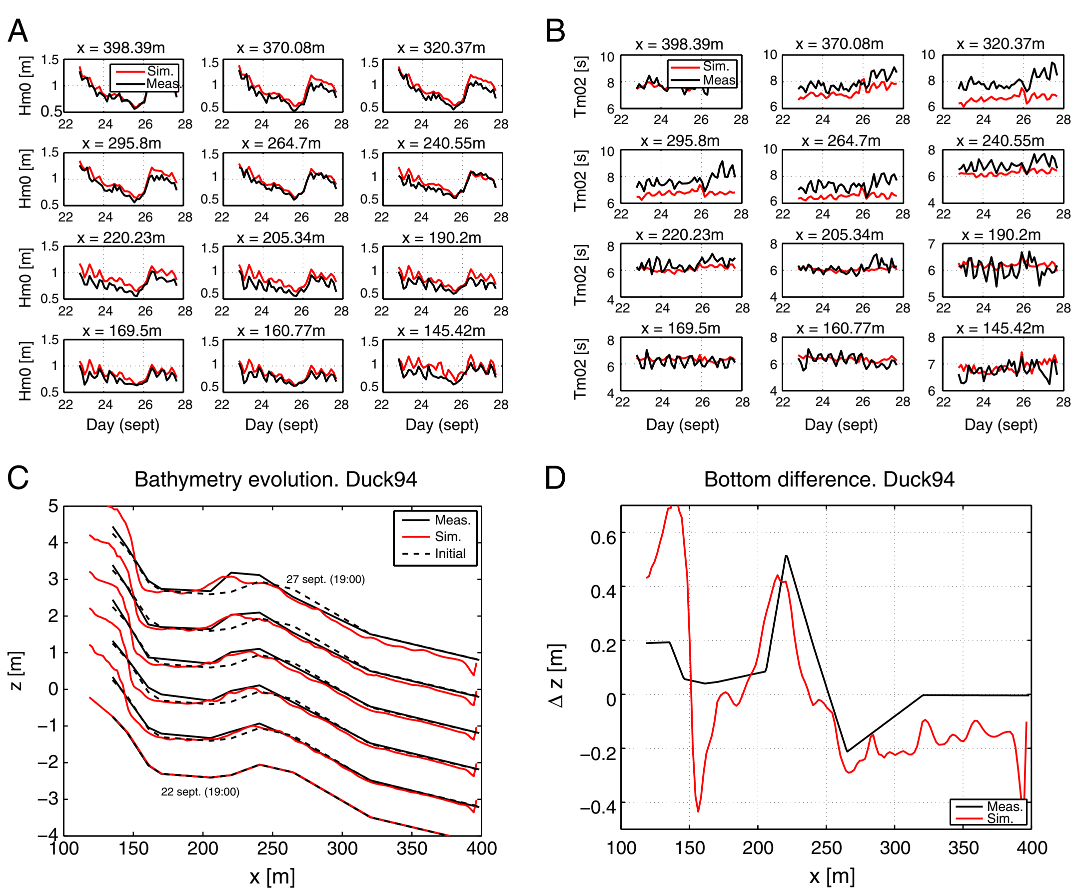

Fig. 12. Model-data comparison for Duck94. Red lines are the model results, and the black lines are measured data: (A) time-dependent behaviour of wave height at various locations; (B) time-dependent behaviour of wave period at various locations; (C) bathymetry evolution at Duck94 on a daily basis (three hour average profiles 19:00–22:00) during period 22–27 Sept. 1994, the shoreline is on the left; (D) bottom difference over studied period.

Table 2
Definition of error parameters.

Parameter	Formula (m = measured, c = computed)	Remarks
Correlation coefficient R^2	$\frac{Cov(m,c)}{\sigma_m \sigma_c}$	$R^2 = 1$ means no scatter, tendency may still be wrong.
Scatter index SCI	$\frac{rms_{c-m}}{\max(rms_m, \lvert\overline{m}\rvert)}$	This is a relative measure of the scatter between model and data. The error is normalized with the maximum of the rms of the data and the absolute value of the mean of the data; this avoids strange results for data with small mean and large variability.
Relative bias	$\frac{\overline{c-m}}{\max(rms_m, \lvert\overline{m}\rvert)}$	This is a relative measure of the bias, normalized in the same way as the Scatter Index.
Brier skill score BSS	$1-\frac{Var(c-m)}{Var(m)}$	This parameter relates the variance of the difference between data and model to the variance of the data. $BSS = 1$ means perfect skill, $BSS = 0$ means no skill, $BSS < 0$ means model is worse than 'no change' scenario. We consider this parameter mainly to judge the skill of the sedimentation/erosion patterns.

morphodynamic model (Delft3D morphology module). The aim of this system of coupled models is to predict near-shore morphology on the time scale of a storm event and the length scale of a few surf zone widths. The phase-resolving 2DH Boussinesq-type wave model TRITON can accurately predict linear effects (wave dispersion, refraction, diffraction) as well as nonlinear effects (wave breaking, wave skewness, wave asymmetry, generation of bound harmonics), of which the latter terms have been shown to be important when modeling morphological evolution in the nearshore. The Delft3D flow module computes currents and long waves by solving for the short-wave averaged 3D shallow water equations, with short-wave averaged wave forcing from TRITON. The Delft3D morphology module computes sediment transport and performs the bathymetry updating. The wave driver TRITON and the two Delft3D modules are coupled online (in a feedback loop), which means that they run simultaneously, in the meanwhile transferring data.

Short-wave averaging of the TRITON momentum equation yields an expression for the total wave force, i.e. the radiation stress gradient. This force is evaluated in TRITON and transferred to the Delft3D flow module, where it is used to obtain the wave-driven flow and the wave setdown/setup. The wave force is split into an organized (body) force and a roller (surface) force. Based on existing expressions, a time-domain expression for the roller force is derived. The roller force is also computed in TRITON, and is transferred to the Delft3D flow module. The roller force acts on the free surface and points shoreward, generating a bottom-dominated return flow, i.e. an undertow profile. The undertow can be being especially large in the breaker zone, and subsequently has a large impact on sediment transport, particularly during offshore bar migration events. TRITON furthermore computes the wave asymmetry term which is used to obtain the wave-related suspended sediment transport in the Delft3D morphology module. The Delft3D morphology module computes, based on the wave asymmetry and the 3D flow profile, the sediment transport and performs the bathymetry updates. The bathymetry updates are transferred back to the Delft3D flow module and TRITON.

Table 3
Summary of results.

Testcase	Parameter	R^2	SCI	Rel. bias	BSS
Boers-1B	Hm0	0.954	0.172	0.109	
	Setdown/up	0.878	0.791	−0.514	
Boers-1C	Hm0	0.976	0.033	0.018	
	Setdown/up	0.948	0.288	−0.064	
Lip-1B	Hrms	0.891	0.078	−0.046	
	Sed/ero	0.798	0.614	−0.208	0.386
Lip-1C	Hrms	0.899	0.034	−0.011	
	Sed/ero	0.632	0.797	0.008	0.203
Duck	Hm0	0.908	0.129	0.102	
	Tm02	0.695	0.098	−0.049	
	Sed/ero	0.710	0.577	−0.255	0.423

The coupling of the wave model TRITON and the Delft3D model is validated by comparing against extensive laboratory data sets (LIP and Boers) and a field case (Duck94). All validation cases feature a barred surf zone with irregular waves. For all cases, the hydrodynamics (wave height, wave spectra, wave setdown/setup, undertow profiles) are predicted fairly well. The wave velocity moments, *guss* and *guls*, are overall predicted well, though there are regions when predictions deviate from the measurements, particularly just shoreward of plunging breakers. In this complicated region, the wave breaking model poorly predicts the cross-shore wave evolution, therefore negatively effecting the subsequent hydrodynamic predictions. Additionally, where the initial wave breaking is predicted, the undertow is over-predicted. Subsequently the suspended sediment concentrations over the crest of the bar are also over-predicted for the lab onshore bar-migration test case.

The model-data comparison shows that the movement of the bar is predicted 'poor', according to Van Rijn et al. (2003), for case LIP-1C (shoreward bar movement), and 'reasonable/fair' for LIP-1B (seaward bar movement) and for Duck94 (shoreward bar movement). For all three cases, the direction of bar migration is correct. For the cases with shoreward bar movement, the largest contribution to the bathymetric changes seems to be provided by the wave-related suspended sediment transport. This quantity is directly related to the wave asymmetry (velocity skewness), which has been shown by others to be a dominate process in onshore bar migration (Lescinski and Özkan-Haller, 2004; Ruessink et al., 2007). Similar to the onshore-bar migration predictions of Long et al. (2006) and Van Maanen et al. (2008), the bar crest did not retain the steep shoreward slope observed in the field measurements of these shoreward-migration events. It is not yet clear what process-interactions result in the development of this steep shoreward face of the onshore migrating sand bar. Van Maanen et al. (2008) proposed that the sand bar could be regarded as a slipface ridge during an onshore migration event.

Summarizing, the bar migration direction was successfully predicted for both onshore and offshore bar migration events in the lab and field test cases. However, the bar shape, specifically the steep shoreward slope of the bar, continues to be predicted poorly for onshore bar migration events, which has consistently been a problem for current nearshore modeling applications (Hoefel and Elgar, 2003; Lescinski and Özkan-Haller, 2004; Long et al., 2006; van Maanen et al., 2008).

Acknowledgements

This study has been funded by the Office of Naval Research under contract N00014-02-C-0075. The authors acknowledge Marien Boers for providing the Boers-1B and Boers-1C measurement data. The authors thanks the anonymous reviewer for his/her useful comments, which have improved the readability and completeness of the paper.

Appendix A. Online separation of a wave signal into a long- and short-wave component

Goal is the separation of the TRITON variable $\varphi=\varphi(t)$, which may represent the surface elevation, the depth-integrated velocity or other quantities, into a slowly varying part (the long-wave or low-frequency component) $\overline{\varphi}=\overline{\varphi}(t)$ and a fluctuating part (the short-wave or high-frequency component) $\varphi'=\varphi'(t)$:

$$\varphi=\overline{\varphi}+\varphi'. \tag{A.1}$$

The long-wave component is also referred to as short-wave averaged component or infra-wave component. The long-wave component is assumed to contain all wave components with a frequency smaller than the separation-frequency f_{sep}, and the short-wave component contains the frequencies larger than f_{sep}. Here, f_{sep} is a user-defined parameter indicating the separation-frequency between 'short' and 'long' waves, the latter including currents. We will design filters that, given a discrete time series of φ, yield $\overline{\varphi}$. Such a filter is called a low-pass filter, because it passes only the low-frequency part, while the high-frequency part is suppressed. The high-frequency fluctuating part then easily follows from Eq. (A.1), i.e. through $\varphi'=\varphi-\overline{\varphi}$.

The separation needs to be performed online, that is, its results are required during the computation. Furthermore, the separation needs to be performed for several variables, on all discrete TRITON time levels and in every grid point. In other words, application of an FFT is not feasible, since this would require storage of large number of time series, each with a length of at least a few wave group periods. This is (a) too memory- and too computing-intensive to perform in each grid cell at each TRITON time step, and (b) assumes some form of stationarity, which prohibits a correct representation of the separated components. In other words, the separation needs to be performed 'on the fly' in time domain, and should – apart from being sufficiently accurate – be computationally cheap.

A way to define a low-pass filter for continuous functions is the following:

$$\overline{\varphi}(t)=\int\kappa(s-t)\varphi(s)ds. \tag{A.2}$$

Here, the function $\kappa(s)$ needs to satisfy the following properties:

- $\kappa(s)=0$ for $s>0$. In other words, only information of the past can be taken into account, because $\overline{\varphi}$ must be evaluated 'on the fly', and not afterwards (as in an ordinary FFT procedure). This leads inevitably to a phase delay: the signal $\overline{\varphi}(t)$ is running behind the low-frequency components in the original signal $\varphi(t)$. Later we will see that we can correct for this to a large extent.
- $\int\kappa(s)d\,s=1$: consistency. For a signal that is constant in time ($\varphi(t)=\varphi_0$), one needs to obtain $\overline{\varphi}=\varphi_0$.
- It seems obvious that $\kappa(s)$ needs to be monotonically increasing for $s\le 0$, i.e. $\kappa(s_1)<\kappa(s_2)$ for $s_1<s_2\le 0$. In this fashion, we ensure that the most recent behaviour of φ contributes most to $\overline{\varphi}$.

A possible choice for $\kappa(s)$ satisfying these properties is the following:

$$\kappa(s)=\begin{cases}2\pi\exp\left(2\pi s/T_{sep}\right)/T_{sep} & s\le 0,\\ 0 & s>0.\end{cases} \tag{A.3}$$

Here T_{sep} is the separation-time, which is an indicative measure for the time over which the history in $\varphi(t)$ makes itself felt. The separation-time and separation-frequency are related through: $T_{sep}=1/f_{sep}$. A nice property of $\kappa(s)$ is that $(d\kappa/ds)/\kappa=constant$; it is this property that makes the recursion introduced later possible.

We need to separate the two components $\overline{\varphi}$ and φ' from a variable φ that is given at discrete time levels. Discretization of Eqs. (A.2) and (A.3), with $\varepsilon=2\pi\Delta t/T_{sep}$ and a constant TRITON time step $\Delta t=t_n-t_{n-1}$, leads to:

$$\begin{aligned}\overline{\varphi}_n&=\sum_{m=0}^{n}\varepsilon\varphi_m\exp[\varepsilon(m-n)]=\\&=\varepsilon\varphi_n+\sum_{m=0}^{n-1}\varepsilon\varphi_m\exp[\varepsilon(m-n)]=\\&=\varepsilon\varphi_n+\exp(-\varepsilon)\sum_{m=0}^{n-1}\varepsilon\varphi_m\exp[\varepsilon(m-(n-1))]=\\&=\varepsilon\varphi_n+\exp(-\varepsilon)\overline{\varphi}_{n-1}.\end{aligned} \tag{A.4}$$

Here, subscript n denotes the time level and $\varphi_n=\varphi(t_n)$ is the computed value of φ at time level $t_n=n\Delta t$. The initial value is specified through the initial conditions: $\varphi_0=\overline{\varphi}_0=\varphi(t_0)$. In expression (A.4), the consistency requirement is violated, because $\varepsilon+\exp(-\varepsilon)\ne 1$. To retrieve consistency, we need to replace the term $\exp(-\varepsilon)$ by $(1-\varepsilon)$. This is indeed the correct thing to do, since $\varepsilon\ll 1$ needs to be satisfied for accuracy reasons, and the Taylor expansion reads: $\exp(-\varepsilon)=1-\varepsilon+O(\varepsilon^2)$. Summarizing, a consistent low-pass filter is given by:

$$\begin{aligned}&\overline{\varphi}_0=\varphi_0,\\&\overline{\varphi}n=\varepsilon\varphi_n+(1-\varepsilon)\overline{\varphi}_{n-1},\quad n=1,2,\ldots,\quad\varepsilon=2\pi\Delta t/T_{sep}\end{aligned} \tag{A.5}$$

We see immediately that application of this procedure is computationally cheap and not memory intensive. Besides φ_n (a TRITON variable that is present anyway), we only need to store variable $\overline{\varphi}_{n-1}$. This value can be overwritten by $\overline{\varphi}_n$ in the time stepping process. Whether the procedure is sufficiently accurate remains to be seen.

It is instructive to derive the same first order filter in a completely different fashion, namely by starting in Fourier space. Let $\Phi=\Phi(f)$, with f the frequency, be the Fourier transform of the (continuous) function $\varphi=\varphi(t)$:

$$\Phi(f)=\int_{-\infty}^{\infty}\varphi(t)e^{-i2\pi ft}dt,\quad\varphi(t)=\int_{-\infty}^{\infty}\Phi(f)e^{i2\pi ft}df. \tag{A.6}$$

We denote this as the Fourier pair $\varphi(t)\leftrightarrow\Phi(f)$. In the same fashion, we define the Fourier pair $\overline{\varphi}(t)\leftrightarrow\overline{\Phi}(f)$. A traditional first-order low-pass filter, see introductory textbooks on signal analysis, is defined as follows:

$$G=\frac{\overline{\Phi}}{\Phi}=\frac{1}{pT_f+1}, \tag{A.7}$$

where G is the transfer function, T_f a filter time constant and $p=if$, with $i^2=-1$. We put the filter time constant equal to the separation-time: $T_f=T_{sep}$. The previously discussed expression can be written in the following form:

$$\left(pT_{sep}+1\right)\overline{\Phi}=\Phi \tag{A.8}$$

Using the relation $d\varphi/dt\leftrightarrow 2\pi p\Phi$, we see that this corresponds to the following ordinary differential equation in time domain:

$$\frac{T_{sep}}{2\pi}\frac{d\overline{\varphi}}{dt}+\overline{\varphi}=\varphi. \tag{A.9}$$

Note that the exact solution to this equation is given by Eqs. (A.2) and (A.3). Discretization of Eq. (A.9) using a mix of forward and backward Euler gives:

$$\frac{T_{sep}}{2\pi}\frac{\overline{\varphi}_n-\overline{\varphi}_{n-1}}{\delta t}+\overline{\varphi}_{n-1}=\varphi_n, \tag{A.10}$$

which is the same as Eq. (A.5). This means that expression (A.5) constitutes a first-order low-pass filter.

One can apply filter (A.5) repetitively, leading to the following algorithm for a filter of order N_f:

$$\begin{aligned}
&\text{Step1}: && \varphi_{(1,n)}=\varepsilon\varphi_{(0,n)}+(1-\varepsilon)\varphi_{(1,n-1)},\\
&\text{Step2}: && \varphi_{(2,n)}=\varepsilon\varphi_{(1,n)}+(1-\varepsilon)\varphi_{(2,n-1)},\\
& && \dots\\
&\text{Step } j: && \varphi_{(j,n)}=\varepsilon\varphi_{(j-1,n)}+(1-\varepsilon)\varphi_{(j,n-1)},\\
& && \dots\\
&\text{Step} N_f: && \varphi_{(N_f,n)}=\varepsilon\varphi_{(N_f-1,n)}+(1-\varepsilon)\varphi_{(N_f,n-1)}
\end{aligned} \tag{A.11}$$

We put $\varphi_{(0,n)}=\varphi_n$ (the original, unfiltered variable at time level n), and we define $\varphi_{(N_f,n)}$ to be the long-wave component $\overline{\varphi}_n$. Starting up the algorithm ($n=0$) in a consistent fashion requires $\varphi_{(j,0)}=\varphi_0$ for all j. We need to store $\varphi_{(j,n-1)}, j=1,\dots,N_f$ in memory, besides φ_n, to get $\overline{\varphi}_n$. In the next time level, $\varphi_{(j,n-1)}$ is overwritten by $\varphi_{(j,n)}$, for all j. It is easy to show that (A.11) constitutes a low-pass filter of order N_f:

$$G=\frac{\overline{\Phi}}{\Phi}=\frac{1}{\left(pT_{sep}+1\right)^{N_f}} \tag{A.12}$$

Because only data from the past is used in Eq. (A.11), the long-wave component $\overline{\varphi}$ (and therefore also the short-wave component φ') is inevitably 'lagging behind' the original (unfiltered) signal φ. In other words, application of a filter such as Eq. (A.12) inevitably leads to a delay time, which is closely related to the phase delay. It is essential, as will be shown later, to account for this delay. The phase delay for filter (A.12) is given by (in radians):

$$\psi_{delay}=\arg(G)=-N_f\,\text{atan}\left(f/f_{sep}\right) \tag{A.13}$$

As we see, the phase delay is a function of the frequency f. This implies that the delay time is a function of frequency also:

$$T_{delay}=\frac{\left|\psi_{delay}\right|}{2\pi}T=\frac{N_f\text{atan}\left(f/f_{sep}\right)}{2\pi f} \tag{A.14}$$

This expression implies that a different delay time should be applied for each wave frequency component. This is impossible, since filter (A.11) operates in time domain and there is no computationally cheap way to distinguish separate frequency components. To circumvent this, the long-wave component is thought to be made up of one frequency component only. This frequency is denoted by f_{lw}, and needs to be specified by the user. The approximation is not a severe one, since the long-wave contribution usually makes up only a relatively small amount of the total signal. Insertion of this approximation into Eq. (A.14) yields:

$$T_{delay}\approx\frac{N_f\text{atan}\left(f_{lw}/f_{sep}\right)}{2\pi f_{lw}}=\frac{N_fT_{lw}\text{atan}\left(T_{sep}/T_{lw}\right)}{2\pi}. \tag{A.15}$$

The delay time is now a constant value, depending only on the user-specified settings for N_f, f_{sep} $(=1/T_{sep})$ and $f_{lw}(=1/T_{lw})$. In case that $f_{lw}\ll f_{sep}$, the term f_{lw} drops out and the previously discussed expression simplifies to:

$$T_{delay}=\frac{N_fT_{sep}}{2\pi}. \tag{A.16}$$

Accounting for the delay time is achieved by letting TRITON run a time lapse equal to T_{delay} ahead of the Delft3D computation. In this fashion, we compensate for the phase delay between the long-wave component as computed by Delft3D and the long-wave component as obtained after filtering the TRITON solution.

The versatility of the separation procedure, including accounting for the delay time, is demonstrated by applying it to a measured wave signal, see Fig. 13. The exact short- and long-wave components in the figures follow from application of an FFT. These serve as a reference solution. The figure shows that the separation procedure based on recursive application of the low-pass filter is sufficiently accurate.

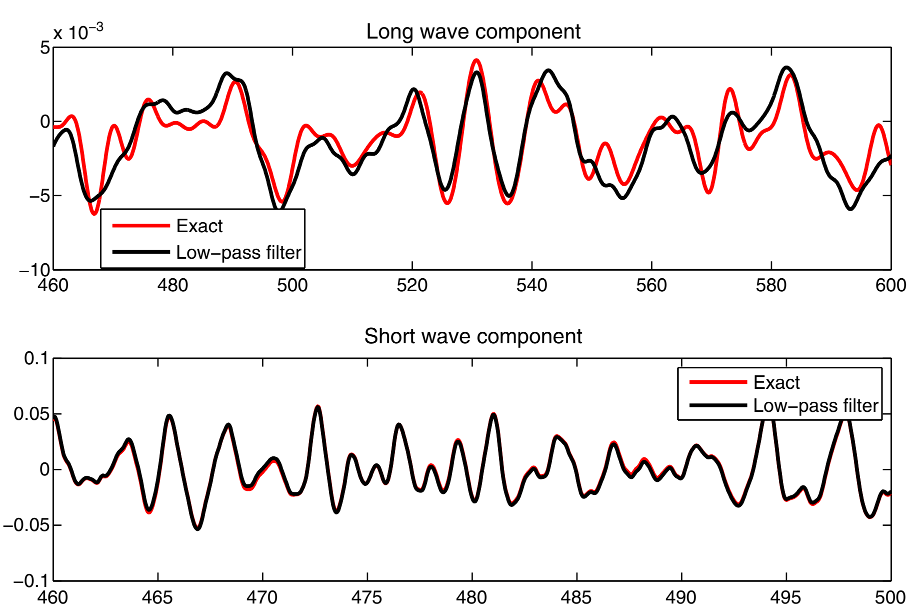

Fig. 13. Application of the separation procedure to a measured time series of the surface elevation. Choice of parameters: $N_f=8$ and $T_{sep}=5.0$ s.

Further experiments have shown that the separation procedure is rather insensitive for variations in the values for f_{sep} and N_f. This is fortunate, since it is not trivial to come up with a theoretically based optimal choice for these parameters.

Summarizing, a cheap (in terms of memory and computational effort) and sufficiently accurate procedure to separate φ into $\overline{\varphi}$ and φ' is obtained.

Appendix B. Estimating the roller force from experimental data

It is possible to estimate the roller force from experimental data. Here, we repeat the discussion of this as given in Section 4.3 of Boers (2005). Depth-integration of the undertow velocities (with linear extrapolation to the mean water level near the free surface) yields the mass flux M:

$$M = -\int_{-h}^{0} \bar{u} dz, \tag{B.1}$$

where $\bar{u}$ is the measured horizontal mean flow velocity. Subtracting the Stokes mass flux (Phillips, 1977)

$$M_s = \frac{E}{\rho c} \tag{B.2}$$

from M, where E is the wave energy, yields the roller mass flux M_r. The roller energy follows from Svendsen (1984b):

$$E_r = \frac{\rho c M_r}{2}. \tag{B.3}$$

The roller energy estimated from experimental data is then inserted into expressions (35) and (36) to obtain an estimate for the roller force:

$$F_r = \frac{\rho g \sin\beta \cdot M_r}{c} \tag{B.4}$$

This procedure yields what is called the measured roller force in Section 5 of this paper. Note furthermore that, since the term $\sin\beta$ occurs both in Eqs. (37) and (B.4) in the same order, the validation of the roller force is not influenced by the choice for the roller angle β (for which we have taken 0.1 rad). However, the magnitude of the roller force, and therefore the undertow, does depend on the size of the roller angle.

Appendix C. Model settings for the validation experiments

In Table 4, the model settings for the validation experiments as discussed in Section 5 are given.

Table 4
Model settings of TRITON and Delft3D for the validation experiments.

Parameter	Boers-1B	Boers-1C	LIP-1B	LIP-1C	Duck
Δx_T (TRITON grid cell size, in meter)	0.05	0.05	0.3	0.5	1.0
Δx_{D3D} (Delft3D grid cell size, in meter)	0.2	0.2	1.0	1.0	2.0
Δt_T (time step TRITON, in seconds)	0.025	0.025	0.1	0.2	0.15
Δt_{D3D} (time step Delft3D, in seconds)	0.6	0.6	1.2	1.2	0.9
f_p (parameter breakermodel)	10	10	10	10	10
ϕ_{ini} (parameter breakermodel)	25	20	25	25	20
ϕ_{end} (parameter breakermodel)	9	8	9	5	5
$t_{1/2}$ (parameter breakermodel)	$T_p/20$	$T_p/20$	$T_p/20$	$T_p/20$	$T_p/20$
f_δ (factor between true and TRITON roller thickness)	7.5	2.5 or 7.5	7.5	2.5	2.5
N_f (order of filter)	8	8	8	8	8
T_{sep} (separation-period, in seconds)	3.3	5.0	8.8	11.8	18.0
T_{lw} (long-wave period, in seconds)	10.0	11.9	21.3	28.6	40.0
T_{delay} (delay time, in seconds)	4.0	6.0	10.6	14.2	21.5

References

Arcilla, A.S., Roelvink, J.A., O'Connor, B.A., Reniers, A.J.H.M., Jimenez, J.A., 1994. The Delta Flume '93 experiment. ASCE, Proc. Coastal Dynamics 1994, Barcelona, Spain, pp. 488–502.

Ardhuin, F., Jenkins, A.D., Belibassakis, K.A., 2008. Commentary on 'The three-dimensional current and surface wave equations' by George Mellor. J. Phys. Oceanogr. 38, 1340–1349.

Boers, M., 1996. Simulation of a Surf Zone with a Barred Beach. Report 1: Wave Heights and Wave Breaking. Communications on Hydraulic and Geotechnical Engineering. 0169-6548.

Boers, M. (2005). Surf zone turbulence. PhD-thesis, Delft University of Technology.

Borsboom, M.J.A., Doorn, N., Groenweg, J., Van Gent, M.R.A., 2000. A Boussinesq-type wave model that conserves both mass and momentum. Proc. 27th ICCE Conference, Sydney, pp. 148–161.

Borsboom, M.J.A., Groeneweg, J., Doorn, N., Van Gent, M.R.A., 2001-aa. Flexible boundary conditions for a Boussinesq-type wave model. Proc. Waves 2001.

Borsboom, M.J.A., Groeneweg, J., Doorn, N., Van Gent, M.R.A., 2001-bb. Near-shore wave simulation with a Boussinesq-type wave model including wave breaking. ASCE, Proc. Coastal Dynamics 2001, Lund, Sweden, pp. 759–768.

Favre, A., 1965. Equations des gaz turbulent compressibles. J. de Mécanique 4, 361–390.

Gallagher, E.L., Elgar, S., Guza, R.T., 1998. J. Geophys. Res. 103 (C2), 3203–3215.

Groeneweg, J., Doorn, N., Borsboom, M.J.A., Van Gent, M.R.A., 2002. Boussinesq-type modeling of measured wave breaking on a circular shoal. Proc. 29th ICCE, ASCE, Cardiff, pp. 495–507.

Henderson, S.M., Allen, J.S., Newberger, P.A., 2004. Nearshore sandbar migration predicted by an eddy-diffusive boundary layer model. J. Geophys. Res. 109, C06024.

Hoefel, F., Elgar, S., 2003. Wave-induced sediment transport and sandbar migration. Science 299, 1885–1887.

Hsu, T.-J., Elgar, S., Guza, R.T., 2006. Wave-induced sediment transport and onshore bar migration. Coastal Eng. 53, 817–824.

Lescinski, J., Özkan-Haller, H.T., 2004. Modeling bar migration using predicted velocity time series. Proc. 29th ICCE, ASCE, Lisbon, Portugal, pp. 2729–2741.

Lesser, G.R., Roelvink, J.A., Van Kester, J.A.T.M., Stelling, G.S., 2004. Development and validation of a three-dimensional morphological model. J. Coastal Res. 51 (2004), 883–915.

Long, W., Kirby, J.T., Hsu, T.-J., 2006. Cross shore sandbar migration predicted by a time domain Boussinesq model incorporating undertow. Proc. 30th ICCE, ASCE, San Diego, USA, pp. 2655–2667.

Mellor, G.L., 2008. The depth-dependent current and wave interaction equations: a revision. J. Phys. Oceanogr. 38, 2587–2596.

Nairn, R.B., Roelvink, J.A., Southgate, H.N., 1990. Transition zone width and implications for modelling surfzone hydrodynamics. Proc. 22nd ICCE, ASCE, pp. 68–81.

Phillips, O.M., 1977. The Dynamics of the Upper Ocean, 2nd edition. Cambridge University Press, London.

Rakha, K.A., Deigaard, R., Brøker, I., 1997. A phase-resolving cross shore sediment transport model for beach profile evolution. Coastal Eng. 31, 231–261.

Reniers, A.J.H.M. (1999). Longshore current dynamics. Ph.D. Dissertation, Communications on Hydraulic and Geotechnical Engineering, Fac. of Civil Engineering and Geosciences, Report no. 99-2, ISSN 0169-6548. 133 p.

Reniers, A.J.H.M., Roelvink, J.A., Thornton, E.B., 2004a. Morphodynamic modelling of an embayed beach under wave group forcing. J. Geophys. Res. 109 (C01030) doi:10.1029/2002JC001586.

Reniers, A.J.H.M., Thornton, E.B., Stanton, T., Roelvink, J.A., 2004b. Vertical flow structure during Sandy Duck: observations and modeling. Coastal Eng. 51 (3), 237–260 May.

Roelvink, J.A., Reniers, A.J.H.M., 1995. LIP 11D Delta Flume Experiments. WL | Delft Hydraulics, Data Report H2130.

Roelvink, J.A., Stive, M.J.F., 1989. Bar-generating cross-shore flow mechanisms on a beach. J. Geophys. Res. 94 (C4), 4785–4800.

Roelvink, J.A., Reniers, A.J.H.M., van Dongeren, A., van Thiel de Vries, J., MsCall, R., Lescinski, J., 2009. Modeling storm impacts on beaches, dunes and barrier islands. Coastal Eng. 56 (11–12), 1133–1152.

Ruessink, B.G., Kuriyama, Y., Reniers, A.J.H.M., Roelvink, J.A., Walstra, D.J.R., 2007. Modeling cross-shore sandbar behaviour on the time scale of weeks. J. Geophys. Res. 112.

Schäffer, H.A., Madsen, P.A., Deigaard, R., 1993. A Boussinesq model for waves breaking in shallow water. Coastal Eng. 20, 185–202.

Shapiro, R., 1970. Smoothing, filtering and boundary effects. Rev. Geophys. Space Phys. 8 (2), 359–387.

Stelling, G.S. (1983). On the construction of computational methods for shallow water flow problems. PhD-thesis, Delft University of Technology.

Sutherland, J., Peet, A.H., Soulsby, R.L., 2004. Evaluating the performance of morphological models. Coastal Eng. 51, 916–939.

Svendsen, I.A., 1984a. Wave heights and set-up in a surfzone. Coastal Eng. 8, 303–329.

Svendsen, I.A., 1984b. Mass flux and undertow in a surfzone. Coastal Eng. 8, 347–365.

Svendsen, I.A., 2005. Introduction to nearshore hydrodynamics. Adv. Ser. Ocean Eng. 24 981-256-142-0.

Trowbridge, J., Young, D., 1989. Sand transport by unbroken water waves under sheet flow conditions. J. Geophys. Res. 94, 10971–10991.

Van Dongeren, A.R., Wenneker, I., Roelvink, D., 2006. A Boussinesq-type wave driver for a morphodynamical model. ICCE 2006, San Diego, USA. Only available on CD-ROM.

Van Gent, M.R.A., Doorn, N., 2001. Wave propagation and wave run-up on dikes with shallow foreshores. ASCE, Proc. Coastal Dynamics 2001, Lund, Sweden, pp. 769–778.

Van Maanen, B., de Ruiter, P.J., Giovanni Coco, K.R., Bryan, B.G. Ruessink, 2008. Onshore sandbar migration at Tairua Beach (New Zealand): numerical simulations and field measurements. Mar. Geol. 253 (7), 99–106.

Van Rijn, L.C., Walstra, D.J.R., Grasmeijer, B., Sutherland, J., Pan, S., Sierra, J.P., 2003. The predictability of cross-shore bed evolution of sandy beaches at the time scale of storms and seasons using process-based profile models. Coastal Eng. 47, 295–327.
Van Rijn, L.C., Walstra, D.J., Van Ormondt, M., 2004. Description of TRANSPOR 2004 (TR2004) and Implementation in Delft3D-online. WL | Delft Hydraulics, Report Z3748.
Walstra, D.J.R., Roelvink, J.A., Groeneweg, J., 2000. Calculation of wave-driven currents in a 3D mean flow model. Proc. 27th ICCE Conference, Sydney, pp. 1050–1063.
Wenneker, I., Borsboom, M.J.A., 2005. A novel Cartesian cut-cell approach. Proceedings Fourth International Symposium on Finite Volumes for Complex Applications. Marrakech, Morocco, pp. 515–524. July.
Wenneker, I., Borsboom, M.J.A., Pinkster, J., Weiler, O., 2006. A Boussinesq-type wave model coupled to a diffraction model to simulate wave-induced ship motion. Proceedings PIANC 31, Estoril, Portugal. Only available on CD-ROM.